SANDIA REPORT

SAND97-0234 • UC-906
Unlimited Release
Printed February 1997

Gated Frequency-Resolved Optical Imaging with an Optical Parametric Amplifier for Medical Applications

Stewart M. Cameron, David E. Bliss

Prepared by
Sandia National Laboratories
Albuquerque, New Mexico 87185 and Livermore, California 94550

Sandia is a multiprogram laboratory operated by Sandia Corporation, a Lockheed Martin Company, for the United States Department of Energy under Contract DE-AC04-94AL85000.

Sandia National Laboratories

Issued by Sandia National Laboratories, operated for the United States Department of Energy by Sandia Corporation.

Available to DOE and DOE contractors from
Office of Scientific and Technical Information
P.O. Box 62
Oak Ridge, TN 37831

Prices available from (615) 576-8401, FTS 626-8401

Available to the public from
National Technical Information Service
U.S. Department of Commerce
5285 Port Royal Rd
Springfield, VA 22161

NTIS price codes
Printed copy: A03
Microfiche copy: A01

SAND97-0234
Unlimited Release
Printed February 1997

Distribution
Category UC-906

Gated frequency-resolved optical imaging with an optical parametric amplifier for medical applications[1]

Stewart M. Cameron
Laser, Optics and Remote Sensing Department

David E. Bliss
Nanostructures and Advanced Materials Chemistry Department

Sandia National Laboratories
P.O. Box 5800
Albuquerque, 87185-1423

Abstract

Implementation of optical imagery in a diffuse inhomogeneous medium such as biological tissue requires an understanding of photon migration and multiple scattering processes which act to randomize pathlength and degrade image quality. The nature of transmitted light from soft tissue ranges from the quasi-coherent properties of the minimally scattered component to the random incoherent light of the diffuse component. Recent experimental approaches have emphasized dynamic path-sensitive imaging measurements with either ultrashort laser pulses (ballistic photons) or amplitude modulated laser light launched into tissue (photon density waves) to increase image resolution and transmissive penetration depth. Ballistic imaging seeks to compensate for these "fog-like" effects by temporally isolating the weak early-arriving image-bearing component from the diffusely scattered background using a subpicosecond optical gate superimposed on the transmitted photon time-of-flight distribution. The authors have developed a broadly wavelength tunable (470 nm -2.4 μm), ultrashort amplifying optical gate for transillumination spectral imaging based on optical parametric amplification in a nonlinear crystal. The time-gated image amplification process exhibits low noise and high sensitivity, with gains greater than 10^4 achievable for low light levels. We report preliminary benchmark experiments in which this system was used to reconstruct, spectrally upcovert, and enhance near-infrared two-dimensional images with feature sizes of 65 $\mu m/mm^2$ in background optical attenuations exceeding 10^{12}. Phase images of test objects exhibiting both absorptive contrast and diffuse scatter were acquired using a self-referencing Shack-Hartmann wavefront sensor in combination with short-pulse quasi-ballistic gating. The sensor employed a lenslet array based on binary optics technology and was sensitive to optical path distortions approaching $\lambda/100$.

Keywords: *ballistic imaging, optical parametric amplification, wavefront sensing, binary optics, tissue spectroscopy, image up-conversion*

* principal investigator to whom correspondence should be addressed
tel: (505)844-4964, fax: (505)844-4045, email: smcamer@sandia.gov

[1]SAND report in support of LDRD case number 3514.050 entitled "Integrated-Optics-Based Ballistic Imaging System for Biomedical Diagnosis."

CONTENTS

(figures incorporated in text)

I. INTRODUCTION

1.1 Motivation:

Noninvasive optical imaging diagnostics to quantitatively measure absorption and scattering characteristics of biological tissues are a fundamental prerequisite for a growing number of physiological monitoring procedures and preventative protocols including: cerebrovascular oxygenation status, photodynamic dosimetry, transillumination shadowography of malignant lesions, and dermatological and ocular photopathology. Although state-of-the art optical imaging performance must be substantially improved to achieve the resolution currently obtainable with conventional radiological modalities such as x-ray computed tomography (CT), positron emission tomography (PET), and magnetic resonance imaging (MRI), optical diagnostics offer unique promise for intraoperative flexibility at significantly lower cost and reduced instrumental complexity in acute care environments. Additionally, probing the near-infrared spectral region (600-1300 nm), or so-called "theraputic window," is a potentially useful noninvasive paradigm for examining internal tissue histopathology owing to the relatively high penetration depths available at these wavelengths with negligible attendant risk of collateral damage from ionizing radiation. The use of optical wavelengths permits dynamic functional imaging of molecular spectroscopic aspects of endogeneous chromophores and blood analytes such as mitochondrial cytochromes and hemoglobin which provide a spatial map or spectral "fingerprint" of tissue physiology and bioenergetics. Structural image information obtained by more traditional invasive methodologies contrastively are predominantly static in nature and are not ideally suitable for condition management or preemptive intervention of progressive disease. Spectroscopic sensitivity to manifestations of neovascularization, microcalcification, cellular architecture, and intracellular metabolic activity associated with carcinogenesis will improve differentiation between malignant and healthy lesions relative to x-rays making detection of carcinomas by remote optical biopsy possible with less ambiguity and improved spatial resolution. For these reasons, the practical realization of an optical transillumination system for examining internal strucure and status of human tissue has broad potential for medical applications, foremost of which are breast cancer diagnosis and in situ monitoring of neurological injury. In this report, we describe a promising new imaging configuration for light-based remote sensing which employs a process known as optical parametric amplification to significantly enhance visualization of embedded structures in biological media. By defeating many of the long standing dynamic range issues which have plagued thick tissue imaging in the past, this approach has the potential to dramatically increase the effectiveness of early-intervention oncological treatment strategies and consequently the prognosis for patient recovery.

1.2 Improved Diagnosis of Breast Cancer

Breast cancer currently accounts for 32% of cancer incidence (182,000 new cases projected annually) and 18% of cancer mortality (46,000 deaths per year) for women in the United States and is the leading cause of death for women aged 40-55, second only to lung cancer for cancer deaths among all women. The continuous climb in the incidence of breast cancer combined with the fast growth of breast carcinomas in relation to the clinical stage of the disease requires systematic and regular screening in the form of x-ray mammograms and physical examinations as the primary intervention strategy to reduce mortality. Although the occurence of breast carcinomas continues to pose a serious health risk, the mortality rate from breast cancer is beginning to decrease due to the efficacy of early-detection mammographic screening protocols and improved awareness regarding oncological management. Unfortunately, as a result of the devastating consequences associated with delayed or misdiagnosis of breast cancer, excisional surgical therapy is often indicated as the safest treatment option for most mammography-detected breast abnormalities even when diagnostic assessment is equivocal. At present, the concensus among medical clinicians is that x-ray mammography offers high sensitivity (95%) of palpable masses, but poor specificity marked by false positive outcomes approaching 40%. The predictive value of a biopsy recommendation is characterized by the sensitivity, or ability of the test to identify correctly who has the disease, versus the specificity, or ability to correctly identify who does not have that disease. This means that a significant number of breast lesions identified radiographically are actually benign or precancerous and do not require surgical intervention, but can not be definitively ruled out solely on the basis of the mammography result. Moreover, the use of x-rays in the mammography process itself is suspected to induce ~.2% of breast cancers creating a conflicting risk-benefit issue for female patients of reproductive age. An excessive false positive rate for benign condition increases screening costs and is a barrier to broad utilization owing to the collective anxiety produced by benign breast biopsies. As a result, cost containment strategies have been emphasized by insurance companies, federal government, and managed care providers, which promote new adjunctive detection methods. Minimally invasive interventional techniques (such as image-guided aspiration cytology) have been sought to decrease morbidity and the number of benign surgical biopsises without compromising the benefits of early breast cancer detection.

Size at Time of Detection (diameter, cm)	Approximate Survival Rate
3	50
2	65
1	80
<1	95

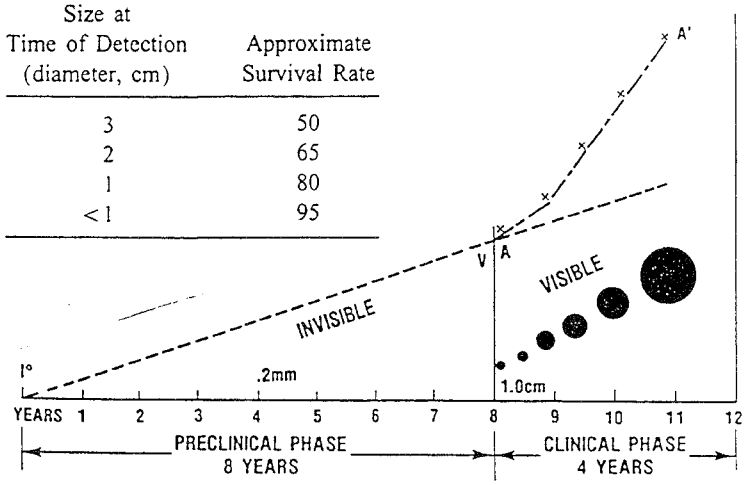

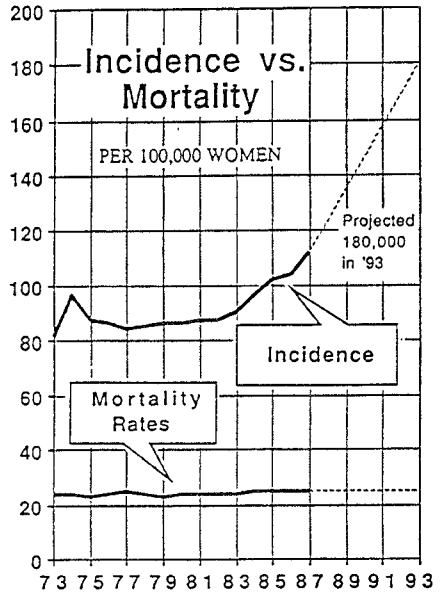

Figure 1: Current state of breast cancer screening, morbidity, and preventative protocol. (a) Incidence and mortality rates per 100,000 women. (b) Calculated life cycle of a generic breast carcinoma with hypothetical doubling period of 100 days showing average tumor diameter as function of time in relation to preclinical and clinical stages of detection. (Source: National Cancer Institute)

Despite advances in digital resolution and contrast enhancement techniques, mammography remains a diagnostic modality where image interpretation is very difficult. Since x-ray scatter contrast between the soft tissues of the breast is inherently low and because relatively minor changes in mammary structure can signify the presence of a malignancy, the detection and interpretation is less objective in mammography than in most other forms of radiography. Suspect signatures are found indirectly in histological markers such as microcalcification, dominate and stellate masses, and the texture of fibrous tissue (fibroglandular patterns) which surround the carcinoma. In some cases, visualizing fine details (~100 μm) at the margins of an area of clinical or pertinent radiographic concern may be crucial to determining the malignancy stage and pathological classification. Microcalcifications associated with in situ intraductal or lobular carcinomas are an important mammographic-pathological correlation indicator because the circumscribed tumor is typically undetectable with x-rays. The neoplasms most overlooked by mammography are embedded in dysplastic tissues of a high radiodensity which adversely affect radiographic visibility. Premenapausal breast tissue in particular poses a challenging problem for early cancer detection because the bulk fibroglandular tissue background exhibits very little adipose content to provide sufficient measurement contrast in x-rays. As a result, the sensitivity and positive predictive value of x-ray mammography is significantly lower in younger women and this shortcoming has caused a recent controversial debate over the advisibility of mammograms in the 40-50 age group. Sonography can accurately identify masses as cystic or solid, but cannot distinguish between benign and malignant masses. Optical transillumination or diaphanography is an alternative approach to radiography which could enhance the ability to identify cancerous lesions early in the preclinical stage before the formation of microcalcification. The ability to distinguish tissue type on the basis of both absorption and scattering properties will help to alleviate interpretational difficulties associated with radiographic density of fibroglandular tissue. As an adjunctive modality together with conventional mammography, optical imaging will improve cancer screening effectiveness for the identification of preclinical stage neoplasms embedded in radiodense dysplastic tissue and reduce the potential danger from mutogenic complications associated with x-ray exposure and radiation hypersensitivity (AT gene) in high-risk groups. This will significantly impact the small percentage of diseased patients under age 35 for which 90% of registered cases are lethal because of late-detection.

A primary breast carcinoma is relatively undifferentiated with close proximity to the lymphatic system and can metastasize when it consists of a relatively small number of cells far below the threshold for detection. Progressive staging of the disease is described by categories denoted (i) in situ, (ii) localized, (iii) regional, and (iv) distant. This nomenclature is applied to invasive malignancies at primary sites and classifies depth of invasion by the

neoplasm on the basis of extension to neighboring tissues and organs, regional lymph node involvement, and common situ metastases. Statistical epidemiology of tumor registry data clearly shows that patient survivability is directly linked to the stage of tumor pathology and size, and an early preclinical diagnosis of a lesion implies a 95% five-year survival rate falling to 72% for regional disease and 18% for distant. Early detection is therefore essential for successful preemptive treatment with minimal surgical intrusion and to relieve associated emotional and psychological stress. Currently the vast majority of suspected breast cancers are found initially by physical examination (palpation) or x-ray screening early in the clinical stage. As shown in figure 1b, the onset of the diagnostically visible or clinical phase (when a tumor diameter of ~ 1 cm is achieved with present technology) of a malignant breast carcinoma is hypothesized to occur on average eight years after inception. By this point in the tumor growth cycle, there is a distinct possibility that active nodal involvement may have already occured and that the disease is no longer localized emphasizing the need for improved detection capability at earlier times. In principle, improvements in spatial localization and contrast are possible with a laser-based optical imaging approach. Combined with the ability to distinguish subtle differences in both scattering and absorption properties of fibrocystic versus normal fibroglandular or adipose breast tissue, and sensitivity to physiological information regarding tissue vascularity and function, optical transillumination will decrease the incidence of false positive outcomes and afford increased lead times prior to metastasis, and may assist in the diagnosis of other tissue abnormalities such as benign cysts and lymph gland inflammation.

1.3 Monitoring of Neurological Function

Another promising medical application for optical imaging is monitoring pathophysiological implications of hypoxic and ischemic neural damage in cases of severe head trauma. Current tools for the evaluation of neurological function are inadequate for early-detection of impending brain injury and for monitoring the time-dependent response of cerebral metabolism to hypoxic and ischemic stress mechanisms. Traditional static imaging approaches including MRI, transcranial ultrasound, and Doppler flowmetry are limited in scope because they are intermittent and do not provide global, temporally-resolved functional images overlaying three-dimensional anatomical structure. Such information is essential for management of degenerative conditions such as stroke and Alzheimer's syndrome, or to guide early-intervention strategies for suppressing superficial bleeding (e.g., subdural hematomas and intraventricular hemorrhage.) The sensitivity of transcranial near-infrared spectroscopy to oxygen-carrying pigments combined with the deep transmissive penetration properties of these wavelengths into human brain tissue establishes a useful diagnostic basis for monitoring oxygenation status and regional asymmetries in the cytochrome system. Exact understanding of variations in regional and global blood flow and associated cerebral metabolism after brain injury would more precisely guide therapeutic intervention and facilitate the measurement of fundamental recovery metrics such as metabolic status, oxygenation, and blood distribution. Early-warning or continuous monitoring capability would ideally involve capacity for intracranial visualization integrated with quantitative spectrophotometric monitoring of %Hb-O_2 saturation state, cerebral blood volume (CBV), blood flow (CBF), and cellular oxygenation state (cyt-O_2).

Cerebral oxygen content is a direct measure of adequacy of oxygen delivery to the brain relative to level of metabolic consumption, and regulated homeostatic mechanisms closely monitor the coupling between cerebral oxygen delivery and consumption under normal conditions. When an imbalance occurs, it can be a direct indication of evolving injury. Ischemic trauma occurs when oxygen delivery falls below consumption due to arterial blockage impeding blood flow to the brain and can result in time-dependent irreversible cell death, paralysis, and permanent damage to cognitive functions. In response to hypoxia (lowered oxygen availability or a blood supply deficiency), progressive vasodilation can lead to decreasing vascular resistance, lowered blood pressure, and subsequently send the patient into shock. The reverse condition, when cerebral oxygen delivery exceeds metabolic requirements, is referred to as hyperemia and has been associated with severe head trauma, post-ischemic reperfusion, cerebral infection, and superficial bleeding (hemorrhage) from a burst vessel into space around the brain. Precise quantification of oxygenation in either scenario would be helpful for delineating symptoms indicative of serious injury risk or brain dysfunction from those inherent to normal postoperative recuperation. The distinction between ischemic and hemorrhagic strokes will affect emergency treatment guidelines for the adminstration of anti-clotting pharmaceutical agents such as tPA which can substantially reduce death and crippling caused by strokes, now the third leading cause of death in the United States. Systematic optical screening of neonates or even premature infants, and coma patients could help to prevent the onset of irreversible debilitating processes in brain or nervous functions, and would be clinically useful in intensive care environments for detecting delayed and recurrent intracranial hematomas. Such measurements would also improve the early detection and treatment of strokes, fast-growing tumors, degeneration of the brain (senility, dementia praecox), and Alzheimer's disease. Monitored cerebral activity

could be used to help diagnose cognitive difficulty (memory, vigilence, perception) related to such disorders as depression, schizophrenia, or even drug addiction so that therapy could be controlled or evaluated continuously.

1.4 Report Organization

The organizational structure of this report is as follows. After a brief overview discussion of motivating factors for a clinical instrument from a medical prospective (section I), the basic phenomenology of light transport in diffusely scattering media relevant to optical imaging is described (section II). The ballistic time-gating concept for imaging objects obscured by turbidity is introduced in section III and realistic operational requirements for a temporally resolved tissue imaging system are identified. Section IV explores the physical basis for optical parametric amplification and reports preliminary experimental data benchmarking dynamic range capabilities and characterizing imaging properties in a functionalized gate geometry. In section V, simple adaptations of the apparatus for phase imaging with lenslet array wavefront sensors are demonstrated. Finally, section VI explores laser source miniaturization strategies using recently developed semiconductor diodes and integrated optical components.

II. OPTICAL SPECTROSCOPY OF TISSUE

2.1 Near-Infrared Absorption Window

The physical basis for light-based biomedical imaging is that variations in absorbance and scattering properties underlying the light-tissue interaction influence photon travel through tissue and are strongly influenced by local chemical composition and cellular structure. The absorptive properties of tissue are largely derived from its constituent chromophores, primarily proteins, nucleic acid residues, hemoglobin, and water as indicated in figure 2. Delocalized $n \rightarrow \pi^*$ and $\pi \rightarrow \pi^*$ electronic transitions associated with the peptide and hydroxyl groups, aromatic amino acid side chains, and purine and pyrimidine bases dominate the ultraviolet absorption spectrum for wavelengths shorter than ~350 nm. Prosthetic groups in hemes and metal protein complexes exhibit near-ultraviolet and visible absorption bands with specific spectral features sensitive to details of ligand coordination chemistry. Hemoglobin exhibits a strong complex absorption spectrum in the blue-green region, decreasing significantly at wavelengths longer than ~600 nm. Near 1300 nm, broad vibrational overtones of water begin to absorb strongly effectively closing the theraputic window for useful optical transmission in thick tissue. Between these wavelengths,

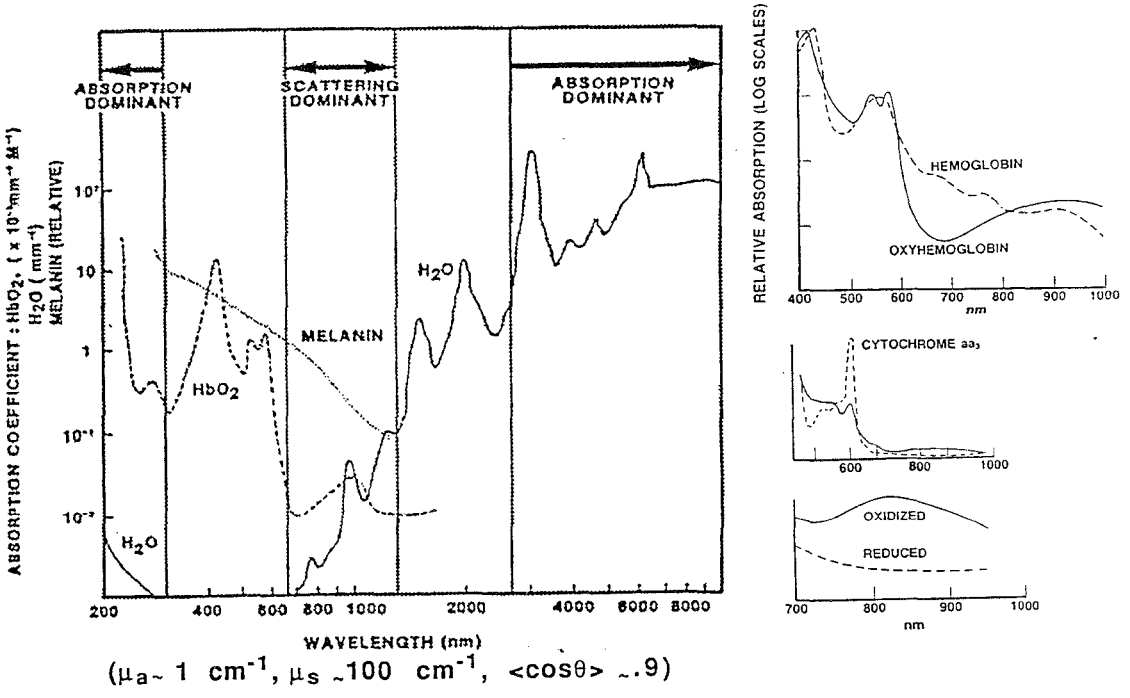

Figure 2 : Absorption spectra for proteins, amino acids, oxygenated Hb, melanin, and water in units of cm^{-1}. The useful theraputic window for optical imaging extends from 600 nm to approximately 1.3 μm.

deep transmissive penetration of optical radiation with decreased absorption due to heme and melanin pigments is possible, while still maintaining useful quantitative spectral sensitivity for differentiating oxygenation ($Hb\text{-}O_2$ ~ 670 nm) and phosphorylation (aa_3 ~ 820 nm) metabolic states. The dominant optical attenuation process in this wavelength interval is Mie scattering which can strongly affect diffuse propagation of the illuminating light field as a function of depth through the tissue. Fortuitously, wavelength and pulsewidth considerations for transillumination of soft tissue appear to overlap well with both solid-state diode and titanium sapphire laser technologies. This should be contrasted with the ultraviolet (excimer) and infrared (erbium) laser sources proposed for laser ablation (eg. angioplasty), photo-coagulation surgery, and photoacoustic/photochemical therapies all of which require efficient coupling with absorption and heat conduction properties of the medium for effectiveness.

2.2 Light Propagation in Biological Media

Although the near-infrared is the spectral region of greatest optical transparency, multiple scattering is pervasive in fatty tissue at these wavelengths and hinders image formation and the distinguishability of absorption. Elastic scattering inhomogeneities originating from cellular components (chromatin, organelles, membrane interfaces, intracellular fluid, solutes such as glucose, etc.) with dimensions on the order of an optical wavelength modify the bulk index of refraction (n=1.35-1.5) and cause strong random diffusion of light. Significant temporal and spatial dispersion is induced by this random scattering process on optical pulses escaping diffuse inhomogeneous (turbid) media such as tissue, and results in a broad distribution of scattering trajectories and associated pathlengths taken in traversing the medium. The nature of transmitted or reflected light ranges from the quasi-coherent properties of the minimally scattered component to the random incoherent light of the diffuse component. Light propagating in tissue will typically lose coherence memory after travelling only a few millimeters from the initially irradiated region with each photon on average having undergone 100-1000 scattering events with an increase in effective pathlength of over tenfold. Diffuse scatter resulting from the presence of these complex photon transport patterns and migration dynamics acts to obscure knowledge of the spatially localized path connecting signal with originating volumetric element, and is the main obstacle to quantitative implementation of optical imagery and tomography in turbid environments. As opposed to conventional radiological methods in which x-ray photon trajectories are dominantly along the instrumental line-of-sight, for the case of optical wavelengths, multiple scattering acts as a fog to produce a broad distribution of optical propagation delays and irregular pathlengths thereby degrading (or blurring) underlying image information and progressively scrambling the geometric correlation between incident and detected light (see figure 3). The resulting pathlength uncertainty associated with the detected signal will adversely effect quantification of absorbance and the accuracy of range-resolved optical sensing measurements derived as a finction of propagation delay time. In addition, the diffuse background level will reduce the effective dynamic range and maximum penetration depths available for unambiguous object detection. Compensation for these "fog-like" effects will require dynamic path-sensitive imaging methods which rely on spatial, temporal, and phase signatures to actively discriminate against diffusely scattered light background and image obscuration .

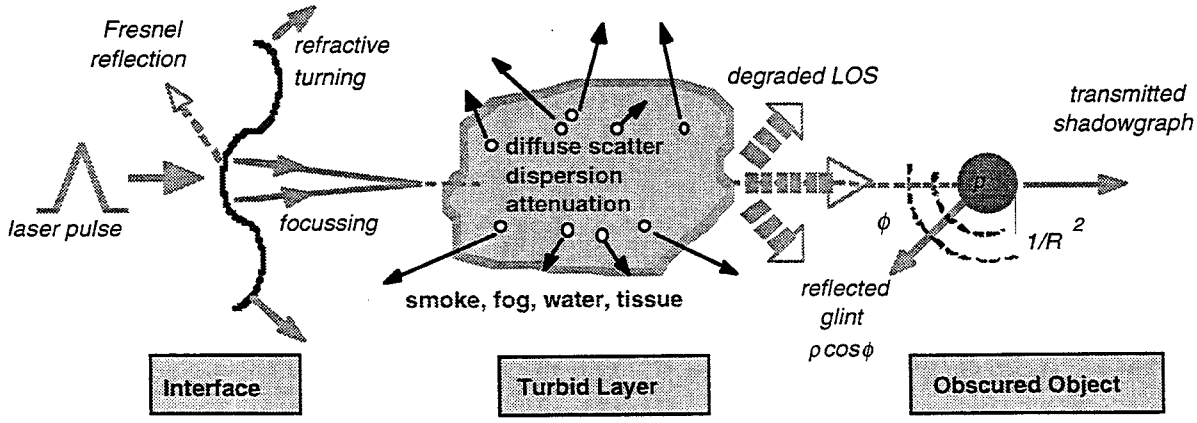

Figure 3: Basic physics issues germane to optical imaging in turbid or low-visibility environments. The presence of diffuse scattering will adversely impact many remote sensing applications including light-based medical diagnostics.

Although the dielectric function (phase and amplitude image) may in principle be reconstructed from the diffuse emission if the spatial and temporal distribution of the phase and amplitude are known simultaneously at many discrete points, the uncertainty of path of the detected signal makes the inverse scattering problem inherently underdetermined in the absence of deterministic constraints (restrictive assumptions) or simple boundary conditions. Computational approaches to model photon fluence propagation in highly scattering media based on the diffusion approximation to radiative transport theory and numerically intensive Monte Carlo particle-in-cell simulations have been similarly difficult to implement for realistic scenarios; i.e., stochastic boundary condition imposed by random interface.

2.3 Oximetry and Optical Pathlength Considerations

In principle, variation in light absorbance and scattering characteristics at different wavelengths can be used to deduce the concentration of physiological intermediates provided the pathlength is accurately known. This capability is premised on a direct quantitative correlation between optical pathlength through the intervening medium, the associated propagation delay, and distance to the object or chromophore. In general there are two distinct aspects to the spectral imaging problem in turbid media owing to the dispersive effects of scattering: path localization and spectral characterization. The variability of optical pathlength in transilluminating biological tissue therefore has a major implication for the study of *in vivo* oxygenation. As with all forms of optical oximetry, quantitative measurement of hemoglobin pigment using near-infrared spectroscopy is based on the premise that changes in the absorbance of light (A) are related to changes in the concentration [C]. In the simplest nonscattering form, the relationship is given by Beer's law; $A=\varepsilon[C]L$. However, in tissue, optical pathlength (L) is increased unpredictably by irregular multiple scattering trajectories to produce a wide range of paths and changes in absorbance. There is both a static and dynamic component to variability of optical pathlength and such variability will necesarily impose limits upon the maximum accuracy that can be achieved during deep tissue imaging spectroscopy unless ongoing dynamical path-compensated measurements are made. Additionally, the extinction coefficient(ε) of many chromophores varies with pH, blood oxygenation, and other morphological factors. Quantification of oxygenation status and other metabolic chromophores will require precise *in situ* determination of optical path and absorbance, and coherence signatures of the emitted light will be needed to untangle random photon paths for meaningful image formation .

2.4 Air-Tissue Interface Effects

The optical response of biological tissue to laser irradiation can be separated into two principal components: coupling losses at the air-tissue interface which are governed by standard geometric optics expressions, and attenuation and radial spreading effects in the bulk which are phenomenologically described according to a point spread function (PSF) formalism derived from small-angle scattering or diffusion theory. The point spread function describes the intensity blur distribution as a function of range from the source and may be obtained from an integral equation invoving the attenuation coefficient and volume scattering function of the media. Incident light rays are propagated and refracted at the index boundary according to Snell's law and the energy transmitted to the interior is reduced by the Fresnel transmission coefficient T=1-R which is a function of the local surface normal and ray angle:

$$R(\theta_i)=(1/2)[\sin^2(\theta_i-\theta_t)/\sin^2(\theta_i+\theta_t) + \tan^2(\theta_i-\theta_t)/\tan^2(\theta_i+\theta_t)] \quad (1)$$

Here θ_i is the angle of incidence on the boundary and the angle of transmission is given by Snell's law using the indices of refraction n_i and n_t of the respective layers:

$$\sin\theta_t = (n_i/n_t)\sin\theta_i \quad (2)$$

For an ideal air-tissue interface (n_a:n_t ~1:1.4) and laser beam geometry normal to the tissue surface, the specular reflection loss is approximately 2.5%. In some cases, surface roughness and spatial inhomogeneities with structure scalelengths $\geq\lambda_{opt}$ can adversely affect imaging of an optical sensor by altering amplitude and phase characteristics of the propagating beam and creating a significant clutter field with enhanced backscatter. Refractive turning (beam steering) and focussing/defocussing induced at the tissue interface or near steep index gradients along the transmitted path results in spatial distortion of the original beam. These perturbations will be partially offset at greater penetration depths because of the combined effects of decreasing curvature and increased blurring by multiple scattering.

2.5 Light Distribution and Transport

A uniform laser beam is attenuated as it propagates through bulk tissue by absorption and scattering according to the general relation

$$\phi_c(z) = E_o \exp(-\mu_t z)(1-R) \tag{3}$$

where E_o is the surface irradiance (W/m^2), μ_t is the attenuation coefficient (m^{-1}), and R is the Fresnel reflection coefficient. Light scattered from the beam is re-scattered until it is absorbed, reemitted (diffuse reflectance), or transmitted (diffuse transmission). Exact modelling of microscopic light transport in tissue is not possible since the tissue volume is inhomogeneous with both discrete and continuous variations in dielectric constant. Instead, optical propagation of scattered light in turbid media is generally described macroscopically by a phenomenological transport equation rather than Maxwell's equations and incorporates fundamental optical interaction coefficients characteristic of photon diffusion: absorption coefficient μ_a, scattering coefficient μ_s, scattering anisotropy (g), and the local refractive index n. The photon transport equation describes changes in the local radiance due to attenuation of light by absorption and/or scattering, and to scattering of light in the direction of interest from other incoming directions. It is assumed that photon scattering and absorption result from independent events and occur at discrete randomly distributed centers in the scattering medium. On this basis, absorption and scattering coefficients within the confines of radiation transfer theory represent the probability per infinitesmal pathlength for a given photon to be absorbed or scattered. The reciprocal quantity or corresponding transport length denotes the mean photon random walk step and is related to the scattering mean free path by $l_t = l_s/(1-g)$ where (g) is the average cosine angle $\langle\cos\theta\rangle$ of scattering contained in the forward scattering phase function (Henyey-Greenstein) describing angular dependence of each scattering event. The quantity l_a is the mean distance a photon travels before being absorbed. Two limiting cases, excluding absorption, serve to illustrate the inherent physical connection between directional symmetry of the scattering process, transport e-folding length, and scattering mean-free-path. For the first case, consider an isotropic (Lambertian) scattering medium in which the size of the scatterer is much smaller than the optical wavelength. Under these conditions, the scattering process has no preferential direction and $g \sim 0$ so that $l_t = l_s$. In the second case for consideration, we choose a forward-scattering anisotropic medium ($g > 0$) in which the size of the scatterer is comparable to the wavelength. This set of conditions is representative of the generic case for tissue, $g \sim .95$ and $l_t \geq 20 l_s$, and produces a distinctly different result from the former limit with important consequences for photon diffusivity. More formally, one can define a transport mean-free-path for forward scattering which includes absorption as $l_t = (\mu_s' + \mu_a)^{-1}$ where $\mu_s' = \mu_s(1-g)$ is the reduced scattering coefficient. These quantities are key parameters in the diffusion theory formalism utilized to describe light propagation in thick turbid media when scattering dominates absorption ($\mu_s >> \mu_a$).

In order to model the light distribution in tissue, one needs to solve the appropriate transport equation using assumptions of underlying optical properties. The general expression for the radiance $L(w/m^2 \cdot sr)$ in direction $\underline{s}$ at position r is given by

$$\nabla \cdot L(\underline{r},\underline{s}) = -\mu_t L(\underline{r},\underline{s}) + \mu_s \int_{4\pi} p(\cos\theta) L(\underline{r},\underline{s}') d\omega' \tag{4}$$

where the total attenuation coefficient $\mu_t = \mu_a + \mu_s$ and $p(\cos\theta)$ is the phase function which describes the probability of scattering from direction $\underline{s}' \rightarrow \underline{s}$, assuming isotropic initial conditions (i.e., scattering is symmetric about the direction along the incident wave). Experimental measurements of transillumination of tissue suggest that the empirical functional form describing the angular destribution of single scattering events closely approximates the analytical expression of Henyey and Greenstein (H-G):

$$p(\theta) = (1/4\pi)\,(1-g^2)/(1+g^2-2g\cos\theta)^{3/2} \tag{5}$$

with previously defined $g = \langle\cos\theta\rangle = \int p(u)\cos(u)du\,[\int p(u)du]^{-1}$ as the independent asymmetry parameter. The H-G phase function replicates the forward peak of Mie scattering theory with good numerical agreement unless the particle radius approaches the optical wavelength, where the scattering resonance exhibits a many lobe pattern and an exact electromagnetic solution in a Legendre polynomial representation is required. Although the H-G phase function reproduces the forward peak of Mie scattering in most cases, it fails to accurately reproduce backscattering behavior. The function monotonically decreases with scattering angle and will not reproduce the predicted

backscattering or glory. This shortcoming can be partially countered using an independently weighted two-term expansion to accomodate peak asymmetry in the forward and backscattering directions.

2.6 The Diffusion Approximation

The exact solution of the full radiative transport equation is not known, but good approximations to the solution exist in certain limits. One such approximation invoked to solve the radiance equation, the diffusion case, is especially well suited for estimating the visible light field in an optically thick medium such as biological tissue where the reduced scattering coefficient dominates absorption $\mu_s(1-g) >> \mu_a$ and the albedo (μ_s/μ_t) approaches unity. In particular, the diffusion approximation neglects coherent radiance and presumes that the radiance distribution or fluence rate at a distance (typically several scattering lengths) from the source at some time after impulse source injection can be represented by a scalar isotropic component plus a vector perturbation term (linear) embodying the transport of radiant flux (i.e, only diffusely scattered light). When these assumptions are integrated into the transport formalism for diffuse photon fluence $\phi(r) = \int_{4\pi} L(r,s')d\omega'$, it can be simplified to yield familiar diffusion or heat flow type equations in either the time (r,t) or frequency domain (r,ω):

$$(n/c)\partial\phi(r,t)/\partial t - \nabla(D\nabla\phi(r,t)) + \mu_a\phi(r,t) = S(r,t)$$

$$-\nabla^2\phi(r,\omega) + k^2\phi(r,\omega) = S(r,\omega) \qquad (6)$$

where S(r) denotes a photon source term, $D=[3(\mu_a + (1-g)\mu_s)]^{-1}$ is the diffusion coefficient, $k=((\mu_a+i\omega/c_n)/D)^{1/2}$ is the complex attenuation coefficient, and (c) is the speed of light in tissue with refractive index (n). The diffusion model neglects coherent optical effects such as diffraction and interference, as well as fluorescence processes. Although no analytical solution for the most general diffusion case exists, closed-form approximations for homogeneous slab and pinhole transillumination geometries have been developed by several authors and are described in the next section. These expressions can be utilized to qualitatively investigate the sensitivity of fluence rate to local variations in absorption and scattering coefficients inside a turbid medium and can be easily assimilated with radiometric noise models. Note that the single scattering (monopath) approximation of the radiative transfer equation, or so-called lidar equation, breaks down as an accurate description in these cases because of modifications to the attenuation coefficient and scatter probabilities needed to account for increased pathlength and enhanced diffuse scatter. Small-angle scattering theory has also been applied to predict temporal broadening of light pulses as a function of average delay (pathlength) at small optical depths in marginally turbid media (μ_s<<) such as clouds and deep ocean water, but this formalism loses validity as a function of increasing turbidity because it does not properly account for the physics governing scattering attenuation of diffusing light displaced from the optic axis.

III. BIOMEDICAL IMAGING OF TISSUE

3.1 General Approaches

Despite the apparent difficulties, photon migration patterns derived from a variety of optical probes have been employed to study the effects of scattering inhomogeneities on optical pathlength in turbid media and several methods for spatial localization and imaging of hidden opaque or translucent objects have been investigated. Recent develoments have emphasized dynamic measurements with either ultrashort laser pulses or high-frequency amplitude modulated laser light launched into tissue. Both time-resolved (ballistic imaging) and phase-resolved techniques in the frequency domain (phase-modulated spectrophotometry) have been shown to be useful path sensitive approaches to image reconstruction and subsurface object characterization, and both yield theoretically equivalent data related by a temporal Fourier transform $I(\rho,t) \Leftrightarrow I(\rho,\omega)$. In the first approach, a short time window is used to constrain pathlength variability in the measurement interval. In the second approach, the phase shift relative to the average delay experienced by photons traversing the tissue is measured as a function of modulation frequency $\theta(\rho,\omega) \sim \omega<L>/c$, effectively the frequency domain equivalent of variable interval time windows. Mathematically the phase shift θ is the Fourier transform of the temporal point spread function measured in the time domain, which is itself the response function of a narrow impulse. Consequently, measurement of pathlength in the temporal domain can be equally accomplished in the corresponding frequency bandwidth spectrum; time and phase variables in this sense are related by the modulation frequency ω.

3.2 Time Versus Frequency Domain

Tradeoffs exist between the temporal and phase-resolved frequency domain approaches to optical imaging in multiple scattering media. The main advantage of frequency domain measurements with modulated light are the detection of the majority of the re-emitted light (diffuse) in the form of photon density waves over large penetration depths. These low-frequency evanescent waves, in contrast with electromagnetic waves, are solutions to the photon diffusion equation and are characterized by a phase velocity and modulation wavelength which are primarily functions of the optical diffusivity. However, the diffuse imaging approach relies on having a prerequisite spectroscopic model for interpretation and the diffuse character of the measurement variable by its very nature makes achieving adequate spatial resolution in the image potentially problematic without the use of phased array sources in an interferometric geometry. The basic strength of time-resolved spectroscopy is that no mathematical manipulation is needed to interpret the raw data since the photon signal reveals the full time-domain distribution of photon travel (time-of-flight) and explicitly determines scattering and absorption properties. In the time domain approach, pathlength is explicitly determined for each detected photon rather than an ensemble average resulting in good spatial localization at the expense of the small signal size associated with measuring only the coherent component. Additionally, all-optical time domain techniques allow examination of sampling timescales corresponding to gigahertz frequencies inaccessible by current frequency domain techniques, albeit at the expense of the instrumental complexity associated with ultrashort optical technology. The instrumentally challenging aspects of short pulse generation and its associated expense has been considerably reduced by recent innovations in diode laser design and integrated optics. In this work, a time-gating approach based on a novel variation of ballistic imaging is adopted and shown to be effective.

3.3 Ballistic Time-Gating Method

Ballistic imaging is a path-sensitive coherent imaging approach designed to overcome the degradative effects of turbidity on traditional line-of-sight methodologies by exploiting the influence of scattering inhomogeneities on the temporal dynamics of photon diffusion. When an ultrashort light pulse travels through a discrete random medium it is temporally dispersed into two components each characterized by uniquely different optical signatures. The first component (ballistic) is strongly attenuated and comprised of those minimally scattered transmitted photons which result from coherent interference of light scattered in the forward direction. These so-called ballistic photons propagate essentially undeviated from the incident straight-line trajectory and carry the least distorted image information and the highest degree of spatial localization regarding optical absorption. The second component encompasses the majority of re-emitted photons and results from incoherent multiple scattering associated with a diffusive random walk process through the intervening medium, subsequently appearing as off-axis background noise (blur) in the image plane. In the time-gated ballistic imaging approach, one seeks to preferentially isolate the early-arriving image-bearing component from the adverse effects of diffuse scattering on image formation using an ultrafast optical gate, typically less than 50 picoseconds in duration, superimposed on the transmitted photon time-of-flight distribution. The conceptual idea behind time-resolved measurements of this general type is to constrain the distribution of possible light paths and corresponding field-of-view to those relatively rare first-arriving paths exhibiting marginal deviation from the optic axis. By introducing time-resolved detection to select a certain fraction of these early photons for analysis and eliminating the integrated diffuse scattering contribution, only the most spatially informational photons relevent to image capture are detected, thereby effectively sharpening the point spread function defining image quality and spatial resolution. Temporal gating rejects or filters out the much larger number of late-arriving photon trajectories resulting from the incoherent diffuse scattering distribution through the medium, thereby eliminating optical pathlength uncertainty over the gate interval. Pictorially, the signal intensity measured over the gate width (integration time) which emerges from the sample will depend on the inherent absorption and scattering properties within an approximately ellipsoidal volume oriented along the transillumination axis. The spatial extent of the ellipsoid is constrained by the volume of all photon paths which are possible in a given time-gated interval, and the size of each traversal section or time slice $\pm\delta\tau=n\delta L/c$ of the volume represents the resulting spatial resolution of the image.

Numerous experimental methods to implement the requisite temporal discrimination have been demonstrated including optical shutters based on transient nonlinear Kerr, photorefractive, or stimulated Raman interactions, "light in flight" interferometric and cross-correlation heterodyne/homodyne gating based on field coherence properties, electronically gated streak camera imaging, and time-correlated single photon counting. Ballistic imaging techniques such as these can achieve close to diffraction-limited resolution but suffer from extremely small signal levelks due to the selective nature of the time-gating process which discards the bulk of the illumination energy to achieve maximum contrast. Moreover, since the intensity of the time-gated coherent component is

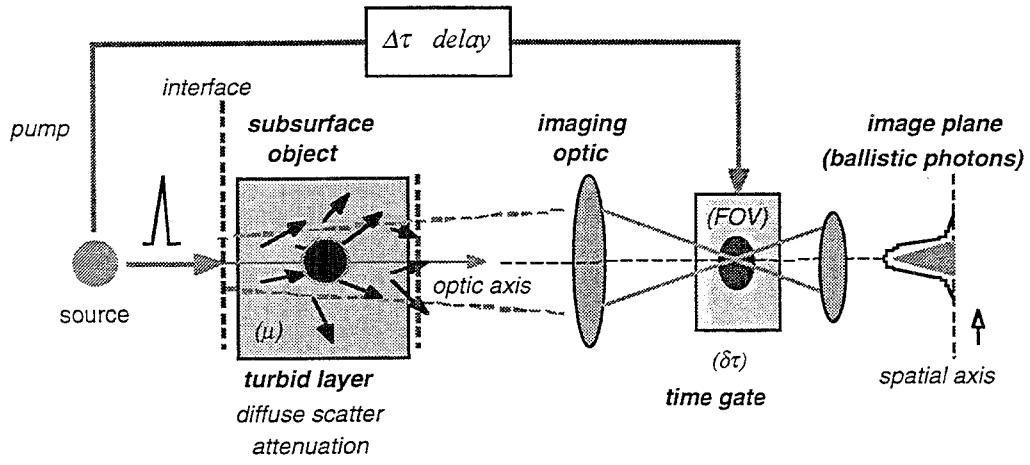

PHOTON TIME-OF-FLIGHT DISTRIBUTION

temporally dispersed pulse

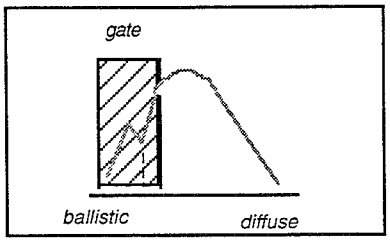

temporally isolate spatially informative image-bearing photons from diffuse background

TIME-CONSTRAINED OPTICAL PATHS

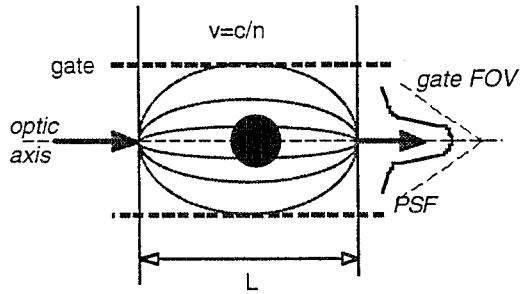

early-arrivng photons least deviated from optic axis (minimal scatter) are detected

Figure 4: Important elements of a ballistically gated transillumination imaging process. The photon time-of-flight distribution illustrates that the time-gate must be superimposed with the early-arriving photons to obtain an image. Finite gate width constrains the allowed optical paths to a narrow loci around the optic axis.

attenuated approximately exponentially with penetration depth and scattering mean-free-path, general applicability is fundamentally restricted in thick scattering media by operational compromises between measurement sensitivity (minimum detectable signal), dosimetry limitations (damage threshold), and image contrast (gate width) criteria.

3.4 Temporal Dispersion

Studies of ultrashort pulse propagation in random media have shown that short duration light pulses escaping an optically turbid medium exhibit a temporal dispersion curve which can be approximately described by a diffusion theory model. The resulting temporal profile of a transmitted impulse viewed through a circular pinhole of diameter (a) on the output face of a scattering medium with thickness L is given by (valid for $L>>l_t$)

$$I(t) = \Omega\,(\pi D/d^2)\,\exp(-vt/l_a)\,[1-\exp(-a^2/4Dt)]\sum_{m=1}^{\infty} m\,\sin(m\pi L/d)\,\exp[-Dt(m\pi/d)^2] \qquad (7)$$

Here $D \sim vl_t/3$ is the diffusion coefficient, $d = L+1.42l_t$ is the extrapolation length, $v = c/n$ is the photon speed in the medium, and Ω is the collection geometry factor proportional to field of view. The expression for the light intensity distribution or PSF at the exiting surface convolved with temporal gate profile (window function) $G(t)$ can be wriiten:

$$I_{tot} = \int_{-\infty}^{t} I(t-t') \otimes G(\Delta t)\, dt' \qquad (8)$$

Total intensity of diffuse light over the full dispersion curve in the absence of temporal discrimination is obtained by applying integration limit $t \to \infty$ to equation (7) with $G(t)= 1$ to yield

$$I_{diff} \sim \Omega \sinh [\, \beta(1- z/d)]/ 2 \sinh (\beta) \qquad (9)$$

where the transport length $l_t = l_s / (1-g)$ has been previously defined and parameter $\beta^2 = 3d^2/l_t l_a$.

As indicated in the previous section, the transmitted photons can be classified into two phenomenological categories based on their respective attenuation properties and time-delay behavior. The first category, or ballistic regime, is not rigorously a solution to the diffusion equation and contains those few photons which have traversed the sample without significant scattering dispersion and consequently arrive at the causal delay time $t_b = nL/c$. In addition to having distinctly different spatial-angular and temporal characteristics from diffuse light, ballistic light retains much of its original coherence properties, and propagates along the optical line-of-sight with an exponential attenuation dependent on the intrinsic absorption and scattering lengths

$$I_{coh} = \Omega \exp[-z(1/l_a + 1/l_s)] \qquad (10)$$

In turbid media, the pure ballistic component is typically eight to ten orders of magnitude smaller than the integrated diffuse background level (eq. 9) depending on the specific optical parameters involved and has a temporal extent comparable to the incident pulse duration. Therefore, some form of gating discrimination utilizing short pulses or confocal apertures is essential to reduce the dominance of diffuse effects and to isolate the weak underlying ballistic signal.

The majority of scattering photons contribute to the diffusion regime which occurs empirically when enough time has elapsed (>twice the causal delay time) that all of the photons arriving at the image plane have undergone significant multiple scattering and delocalization. In a complex inhomogeneous scattering medium such as

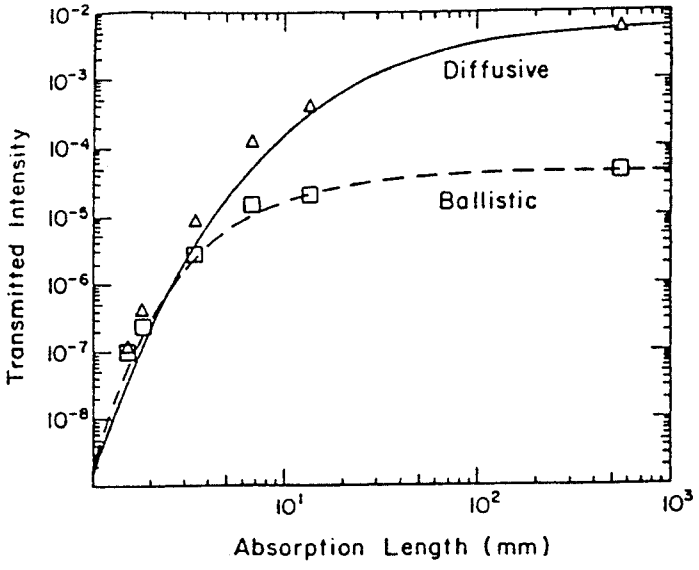

Figure 5: Transmitted diffusive and ballistic intensities calculated from transport theory as a function of absorption length l_a for z=10 mm, l_s=.3 mm and l_t= 1.0 mm . Attenuation due to absorption is favored over scattering and provides a contrast mechanism in tissue (Source: Alfano).

biological tissue, photons will sample both continuous and discrete variation of dielectric constant along the line of least optical path so that the ballistic feature broadens to encompass the quasi-coherent, early-arriving diffuse light and is no longer distinguishable on the time axis. Attenuation properties of early-arriving diffuse light are strongly dependent on the temporal gating interval and can only be described empirically for intermediate time windows. Compared with the ballistic component, early-arriving diffuse light attenuates more gradually as a function of tissue thickness with an exponential decay factor $\sim z/l_t$. The majority of useful early-arriving photons termed "snake photons" do not strictly obey diffusion statistics and traverse the tissue in various zigzag paths that deviate slightly from the straight-line path. Assuming a rectangular gate width Δt,

$$I_{snake}(\Delta t) \sim \int_{t_b}^{t_b+\Delta t} I(t)\, dt \sim I_o\, \Omega \exp(-bL/l_t) \tag{11}$$

and $b \sim l_t/20l_s$ is the modified exponential correction factor typical for a forward scattering process in fatty breast tissue. Note that there is an important distinction between early-arriving diffuse photons which are properly solutions to the diffusion equation (parameterized by l_t) and first-arriving snake (non-ballistic) photons (intermediate parameterization between l_s and l_t) which are not in general a valid solution. Nonetheless, these snake photons are affected by scattering characteristics along their path and can retain enough phase and spatial coherence to permit resolved imaging over greater penetration depths than those possible with pure ballistic photons, although with reduced resolution. By combining spatial filtering and time gating, the ballistic, snake, and diffuse components can be separated by an optical Fourier transform. At the transform plane, ballistic and snake photons will appear as intensity in the central dc (null) spatial frequency range whereas diffuse photons with higher spatial frequencies will be rejected off-axis to a degree determined by the extent of apodization.

3. 5 Image Contrast Mechanisms .

The formation of an image by time-resolved transillumination is mainly due to differential transmittance of the propagating light which is strongly influenced by the internal tissue architecture. Differences in scattering and absorption coefficients will render contrast between tumor and normal tissue, and as a result ballistic and early-arriving light to a lesser degree will form shadowgraph images of embedded absorptive structures within the scattering media. In the case of neovascularization surrounding a tumor, strong perfusion will form a shadow at the hemoglobin absorption wavelength compared to neighboring translucent tissue entities such as bone, adipose, or skin. If light-absorbing lesions are present in tissue, the transmitted signal will be predictively modified as a function of position of the heterogeneity. Compared with the time distribution obtained without an inhomogeneity, the presence of one opaque object on the optical axis (lesion in central plane) will obstruct the transmitted quasi-coherent output and a degraded image will form preferentially with multiply scattered photons since the ballistic photons are absorbed. (i.e., attenuation due to absorption is favored over attenuation due to scattering) Alternatively, when two objects are present displaced on either side of the optic axis the output signal decays abruptly reflecting the predominance of ballistic photons in the image formation process. In general, ballistic and minimally scattered photons are mainly affected by central absorption whereas multiple scattered photons are influenced by peripheral absorption.. Therefore by using information carried by narrow regions of output signal in relation to the position of a heterogenity, time-resolved imaging can influence resolution and contrast.

3.6 Operational Requirements for Time-Resolved Imaging Systems

Since the intensity of the coherent component is attenuated approximately exponentially with thickness and scattering mean free path, the ability to image through dense scattering medium is fundamentally limited by the measurement sensitivity to small ballistic and quasi-ballistic signals. Achievable image quality is a subjective compromise between minimum detectable signal and the relative size of the diffuse component. The gate should provide substantial discrimination against the time-delayed diffusively scattered light which contains the bulk of the pulse energy, while maintaining high transmission efficiency of the image-bearing component for maximum dynamic range. Shorter gate durations imply better image contrast and improved spatial resolution, but at the expense of fewer integrated photons for signal processing. An optimum integration time has to be determined between a blurred dc image (integration time too long) and noisy image (integration time too short). The minimum detectable transmission level for ballistic imaging is fundamentally limited by the quantum shot noise of the detector, and the maximum permissible number of input photons impinging on the tissue sample is limited by dosimetry constraints determined by the ANSI exposure standards and FDA ocular safety guidelines.

The fundamantal transmission limit of pure ballistic imaging is set by the quantum shot noise of the detector and is given for a signal-to-noise ratio of unity as

$$L=\mu_t^{-1}\ln(Eq_{eff}/2h\nu) \tag{12}$$

with exponential attenuation constant $\mu_t(\lambda)=\mu_a+\mu_s(1-g)$, optical energy ($E$) delivered per spatial resolution element, photon energy hν, and photocathode quantum efficiency q_{eff}. Typical optical parameters for fatty or fibroglandular breast tissue at 800 nm are $\mu_a\sim 1\ cm^{-1}$, $\mu_s\sim 100\ cm^{-1}$, and Mie anisotropy $g=\langle\cos\theta\rangle\sim.9$. The maximum ballistic imaging thickness (L) for time gating can be estimated from the burn standard for optical damage to tissue which limits the value of E to a maximum permissible exposure $\sim 1.7t^{1/4}$ J/cm^2 where t is the exposure duration (sec). For a maximum safe energy per pixel of ~2mJ distributed over a 100x100 pixel image, with 10 minute acquisition time, and 500 μm spatial resolution, the unscattered ballistic signal is reduced to the shot noise level when μL~40 mfp which corresponds to ~4 mm in soft tissue. Since all assumed parameters except the mean free path appear in the logarithm, this formulation is a robust estimate which absolutely limits the applicability of pure ballistic imaging to relatively thin epithelial samples given known tissue damage thresholds, reasonable acquisition times, and fundamental quantum noise considerations.

3.6 Resolution and Signal-to Noise Ratio

Optical imaging through greater tissue thickness is possible but requires the use of early-arriving diffuse (or "snake") photons that have undergone at least some degree of scattering thereby compromising achievable spatial resolution. For short gate intervals, these photons benefit from transport length scaling in the exponential $\sim z/l_t$ which can be as much as a factor of ten weaker than the ballistic component case and retain enough phase and spatial coherence to permit coherent detection. Another approach to increase the number of transmitted photons and effective penetration depth is to use longer illumination wavelengths within the theraputic window (low absorption) where the tissue damage threshold increases (x5 factor for $\lambda>1.06$ μm) and the scattering coefficient ($\sigma_{scat}^2\sim\lambda^{-1}$) is reduced. A quantitative expression for maximum diffuse imaging thickness is difficult to determine since it depends on empirical variables such as gate width, illumination/detection geometry, and specific evaluation criteria concerning the quality of the time-resolved image. Small changes in the scattering cross section will sensitively affect the optimum delay time for a given level of resolution and the gate width is also expected to change depending on the number of transmitted photons within the integration time necessary to exceed the fundamental limit of detector response and form an informative image. In general, however, spatial resolution of features located in the midplane of a rectangular scattering medium should be linearly proportional to the maximum possible displacement of photons r_{max} located within that plane which is a function constrained by the integration time. Theoretical studies based on the diffusion approximation, Monte-Carlo simulation, and random path models have shown that the curve describing resolution Δx (width of PSF) capability of an imaging process as a function of integration time $\Delta\tau$ and sample thickness z_{max} follows an asymptotic square root behavior

$$\Delta x\sim[c_n\cdot\Delta t+z_{max}][1-z_{max}^2/(c_n\Delta t+z_{max})^2]^{1/2}\sim 2r_{max}/\beta \tag{13}$$

where c_n is the speed of light in the medium and β is a constant of proportionality (μ_a,μ_s'). The range of applicable integration times is delineated conceptually in figure 6 which depicts general transillumination resolution curves for two different scattering cases. In the absence of anatomical noise, best achievable resolution is theoretically obtained with the shortest experimentally viable gatewidth which is inherently constrained by the combinative effects of illumination dosimetry and the fundamental quantum noise of the detector. As the scattering attenuation μ_s increases (more turbidity), the practical range of useful gatewidths fulfilling this criteria decreases and the resulting resolution degrades toward the diffuse (no gate) limit defined as the half-width (1/e) point of the Gaussian point spread function. Similar curve shapes are obtained using holography or white light interferometry where instead of integration time, resolution is plotted as function of coherence time of the reference pulse. In this case, interference occurs only when the propagation phase delay is less than the coherence time τ_c which is inversely related to the source spectral width.

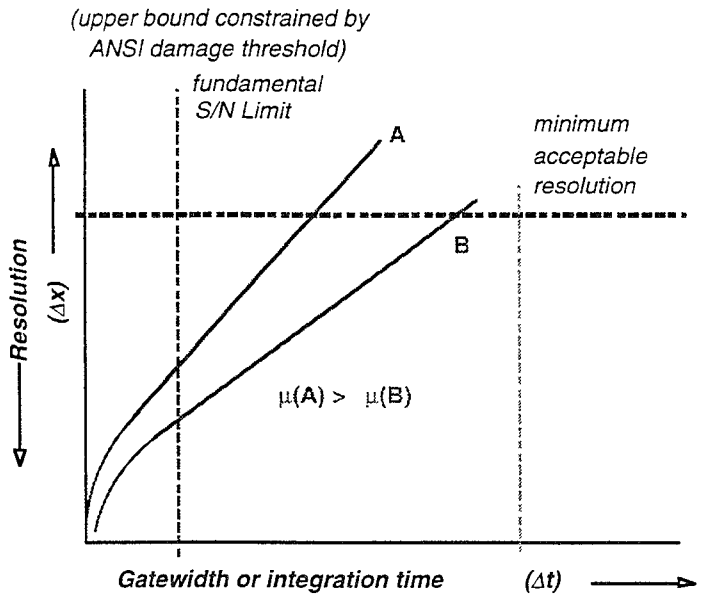

Figure 6: General spatial resolution considerations in quasi-ballistic transillumination imaging as a function of integration time (gatewidth) for two samples $\mu_s(A) > \mu_s(B)$ in the absence of noise. The asymptote as $\Delta t \rightarrow \infty$ defines diffuse behavior and minimum resolution.

An image quality index (IQI) or predictor based on decision theory has been developed by radiologists to establish a more rigorous quantitative resolution criterion defining object detectability. This calculation can be performed from knowledge of the line spread function (LSF) of the imaging system, the noise pattern $W(\Delta t)$ of the image background, and the contrast function $C(\Delta t)$ of the imaged object. In first approximation, the IQI value is proportional to the square root of the sum of Gaussian LSF variance (σ^2) and the noise amplitude given by the integral of the assumed Wiener (white noise) spectrum

$$\Delta x \sim 2[\sigma^2(\Delta t) + \gamma\sqrt{W(\Delta t) / C(\Delta t)}]^{1/2} \tag{14}$$

with a correcting constant γ which is a function of the estimated signal-to-noise ratio (S/N) for high detection probability (i.e., threshold of detection). The contrast (C) has been defined for purposes of calculation of ICI as the difference of signal intensity transmission per unit length by analogy to x-ray attenuation in mammography. As applied to optical transillumination measurements, $C = \Delta OD/z$ (mm^{-1}) would denote the difference in optical density as a function of thickness between tissue types such as adipose and carcinoma. Larger contrast implies a more robost tolerance for noise in the image and occurs for short integration times. For thicker samples, the position of the minimal IQI value is shifted to longer integration times and reduced resolution. In figure 7, the relationship of various tissue optical properties to the image formation process and obtainable IQI are shown schematically.

Note that the useable signal for very short gate times is strongly occulted by noise as seen by the rapid rise in the IQI as $\Delta t \rightarrow 0$. This non-intuitive behavior can be explained on the basis of the interplay of noise statistics with the sharpening mechanism of the LSF when the time-window goes to zero. Although resolution and image contrast of an embedded object theoretically improve as the integration time is decreased, ideally approaching the pure ballistic limit, the S/N ratio simultaneously decreases due to noise augmentation from superimposed small-scale anatomical inhomogeneities and quantum sources which were previously washed out for longer intergation times. As the width of the gating window diminishes, time-resolved detection reduces the number of collected photons and effectively decreases the S/N on each pixel, thereby accentuating noise features which offset the expected gains in image quality.

To obtain the best possible compromise between spatial resolution and IQI noise issues, one should use a temporally narrow ranging pulse for maximum achievable spatial resolution in conjunction with a optimizable variable gate width to preserve detectability of the temporally dispersed output. One powerful technique to achieve

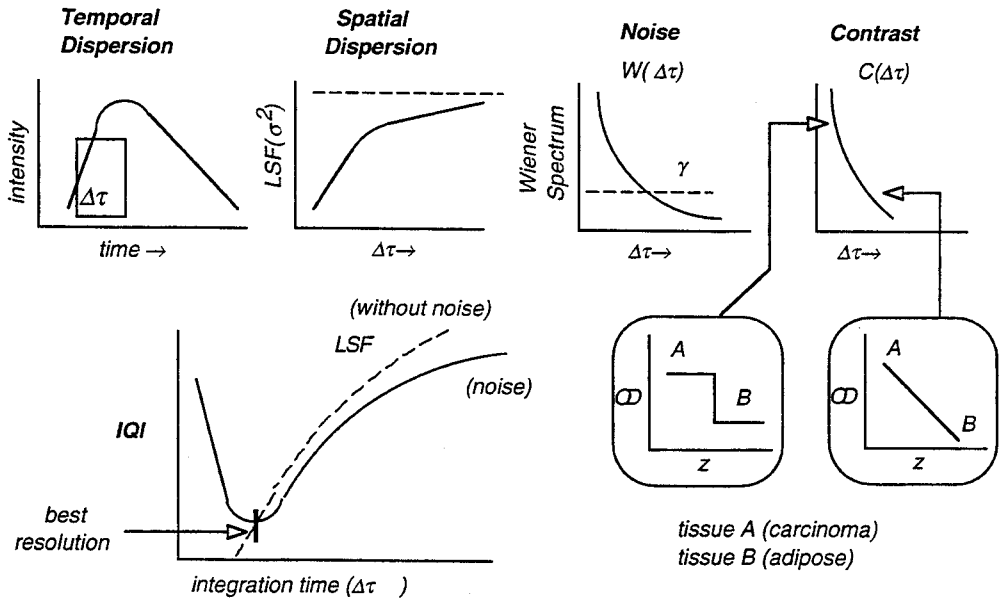

Figure 7: Conceptualized value of the IQI versus integration time and relation to *in vivo* optical properties in the imaging medium; for a 20 mm thick slab of breast tissue with μ_a=.07 mm^{-1} and μ_s= 17.2 mm^{-1} temporal dispersion ~ 1 ns and the IQI minimum will occur at ~30-40 ps for <1 cm resolution.

the experimental flexibility needed to synthesize adjustable femtosecond optical waveforms for this application is to employ phase and amplitude masking of spatially dispersed optical frequency components in a nondispersive grating apparatus (identical gratings placed at focal plane of unit magnification confocal lens pair). In this method, an optical pulse is first transformed from the time domain to the frequency domain and a frequency-dependent complex linear filter such as a slit that modifies the spectrum of the pulse is then applied. Finally the pulse is transformed back into time domain and the resulting output pulse has a temporal field profile that is essentially the Fourier transform of the frequency filter imposed on the electric field spectrum of the pulse. Another advantage of this approach is that pulse broadening due to normal dispersion which can adversely effect longitudinal resolution can be actively compensated by adjusting the chirp of the probe pulse.

3.7 Instrumentation Considerations

Based on a detectable photon flux of ~fW (10^3 photons-sec^{-1}), early-arriving diffuse imaging with a gate width Δt~10-20 ps should marginally be able to measure a signal through a 3-5 cm thickness (reasonable breast compression) of nonabsorbing material with μ_s'< .7 mm^{-1} and maintain close to sub-centimeter resolution. If absorption is present at the level of μ_a~ .05 mm^{-1} an additional attenuation factor of twelve will be incurred over the full thickness, although absorptive contrast can in some instances act to increase the spatial resolution produced in a given integration time. Further signal reductions are to be expected in realistic biological systems which typically exhibit significant structural heterogeneity. Based on these considerations and typical tissue parameters, a transillumination imaging system for biological tissue should ideally be capable of detecting spatially-resolved images over a dynamic range of transmitted signal exceeding twelve orders of magnitude (one photon detectable in 10^{10} launched). The laser source should generate low-noise stable optical pulses at kilohertz or higher repetition rates and deliver ~25 milliwatt average powers to achieve illumination fluences adequate for image contrast over a range of penetration depths (centimeters) while maintaining sample exposure levels below the burn standard for living tissue. The source should possess wavelength versatility for spectroscopic imaging and optimization, and produce the pulse durations necessary to achieve sub-centimeter spatial resolution with sufficient power for nonlinear gating of full 2-D images. One way to improve upon noise limitations in optical transillumination of thick tissue might be to use supplementary anatomical overlays acquired by other imaging modalities such as MRI and ultrasound in conjunction with digital enhancement techniques. In addition, the optical properties of brain tissue are believed to be more favorable for transmission of near-infrared light than fatty soft tissue. It has recently been

suggested that nerve tissue in the brain white matter could exhibit orientation dependent waveguide-like properties which could effectively channel optical radiation to greater depths.

The first-arriving method could be carried out in two imaging modes: broadbeam illumination, and confocal scanning depending on laser output characteristics and field-of-view requirements. Fast sampling achievable with modelocked pulse trains combined with a noiseless amplifying gate could partially compensate for the extremely low number of photons integrated over a short gating periods by improving image processing rates, and minimizing the effect of dark noise statistical fluctuations on photon counting precision and radiometric fidelity of photodetector arrays. Image processing speed is essential for medical diagnosis under conditions where the measurement must be performed rapidly compared to movement of the subject (i.e., motion-induced artifacts due to breathing). In the remainder of this report, the authors will describe a versatile new ballistic imaging configuration for light-based remote sensing of scattering media which integrates an all-optical image intensifier function based on parametric amplification in a nonlinear crystal with temporal gating and wavelength tuning capabilities. The amplifying gate achieves substantial discrimination against time-delayed diffusely scattered light while maintaining high transmission efficiency of the underlying coherent image-bearing component as a function of gain. Expanded dynamic range characteristics offset previous limitations on the detectability of low-level signals resulting from strong multiple scattering or from the restrictive gate widths necessary to achieve maximum image contrast. The gain wavelength can be independently adjusted over the crystal phasematching curve to optimize the response of the system for variable absorption and scattering properties, and in combination with a wavefront sensor, the time-gated amplification process can be adapted to simultaneously acquire phase and amplitude attributes of the intrinsic dielectric function.

IV. TRANSILLUMINATION IMAGING WITH AN OPTICAL PARAMETRIC AMPLIFIER

4.1 Overview of the OPA gate

The authors have demonstrated a wavelength-tunable, ultrashort amplifying gate functionalzed for quasi-ballistic imaging applications based on optical parametric amplification. Parametric amplification, also referred to as difference mixing generation, is of particular interest not only because it is a high gain process which can defeat small-signal detection limitations, but also because the time during which amplification occurs can be effectively limited by the duration of an applied pump (gating) pulse. A short-pulse optical parametric amplifier is capable of ultrasfast temporal gating, direct two-dimensional image acquisition and spectral conversion over a broad wavelength range defined by the signal/idler tuning curve, quantum sensitivity approaching one photon per spatial resolution element, and a high degree of coherent discrimination against diffuse light obscuration of image quality.

As shown schematically in figure 8, the gating mechanism involves the temporal and spatial overlap of a strong reference (gating) beam with the attenuated image-bearing probe beam in a phasematched nonlinear crystal to produce gain via a three-wave parametric $\chi^{(2)}$ interaction. In this process, each incident pump photon pairwise generates two tunable lower frequency photons denoted signal (ω_S) and idler (ω_i) subject to momentum and energy conservation conditions with gain scaling dependent on the crystal interaction length (L) and nonlinearity (d_{eff}), pump intensity (I_p), and phase mismatch (Δk). The gate acts as a noiseless image intensifier (in the absence of spontaneous parametric scattering) to simultaneously amplify and temporally isolate the weak quasi-ballistic or early-arriving partially coherent component of the transmitted light. Gain in the amplifier exists for approximately the duration of the pump pulse and the nature of the nonlinear optical coupling- primarily the time correlation, angular acceptance, and phasematching- provides temporal, spatial, and polarization discrimination against diffusely scattered background light.

The resultant image can be observed directly at the injected probe frequency (image amplification) or alternatively on a zero background at the spectrally converted difference frequency between pump and probe (sideband image upconversion). Time-gated parametric amplification exhibits low noise and high sensitivity, with gains in excess of 10^4 achievable for low incident light levels. Broad wavelength tuning can be accomplished by systematic variation of the crystal phasematching conditions to minimize momentum mismatch and maximize gain, and depth profiling is accomplished by monitoring the transmitted amplitude during the optically-delayed amplification interval set by the gating pulse width $\Delta\tau$; i.e., the detector views a layer corresponding to the gate width. Each time slice of the transmitted pulse contains depth information (100 fs=30μm) and a three-dimensional reconstruction (tomograph) can be progressively built up by stacking sequential images at appropriate delays using a filtered backprojection CT algorithm. The lateral image spatial resolution is determined by the spatial magnification of the gating pulse for the

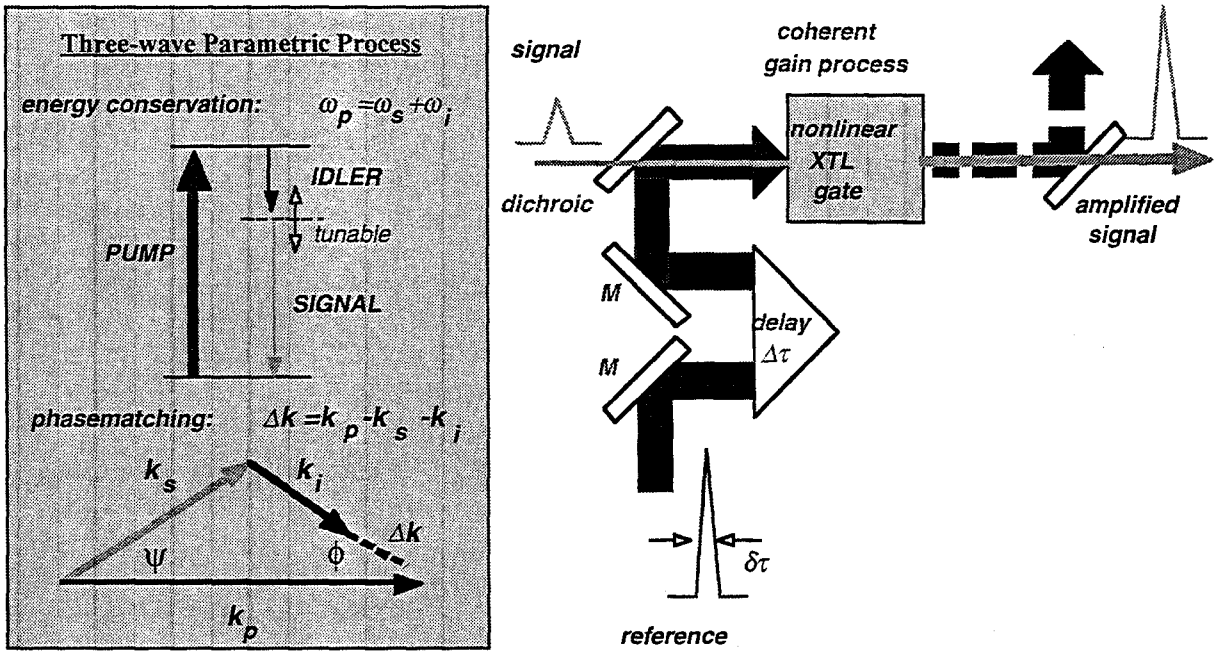

Figure 8: Overview of an optical parametric amplifier realized as a time-gate for quasi-ballistic imaging. Energy from the pump beam is transferred to the signal and idler branches such that energy and phase in all three coupled waves is conserved.

specific crystal focussing geometry defining the gain region, and the longitudinal (depth) resolution is fixed by the incident pulse duration $\delta\tau$. Contrast of the gate is defined by the ratio of light transmitted when the reference beam is present to the off condition .

4.2 Gain Equations

General principles governing the optical parametric conversion process have been previously derived in several critical reviews and mongraphs. Here only a brief overview of the relevant physics fundamental to gate design and short pulse propogation/dispersion engineering issues will be presented. Parametric mixing can be analytically described in the plane wave approximation neglecting pump depletion using the coupled amplitude equations for the pump, signal, and idler field envelopes denoted by subscripts p, s, and i, respectively. The solution for growth (amplification) of the signal wave with no idler initially present, allowing for phase velocity mismatch ($\Delta k = k_p - k_s - k_i$), is given for a lossless (α assumed negligible) crystal of length L as

$$E_S(L) = E_S(0)[\cosh(gL) - (i\Delta k/2g)\sinh(gL)] \exp(i\Delta kL/2) \quad (15)$$

where coupling parameter g is defined

$$g = [\Gamma^2 - (\Delta k/2)^2]^{1/2} \quad (16)$$

and the gain coefficient Γ is given:

$$\Gamma^2 = 8\pi^2 |d_{eff}|^2 I_p / (\varepsilon_o \lambda_i \lambda_s n_s n_i n_p c). \quad (17)$$

Here d_{eff} is the effective nonlinearity of the crystal, ε_o is the permittivity of free space, $n_j(\lambda_j)$is the refractive index (wavelength) of the jth wave, and $I_p = n_p \varepsilon_o c |E_p|^2/2$ is the pump intensity. Concurrent growth of the idler wave in the parametric interaction process will be described by a complimentary equation (interchange subscripts $i \Leftrightarrow s$) and

for the down-conversion process ($\omega_p \rightarrow \omega_s + \omega_i$) , the relative power change in each beam satisfies the Manley-Rowe relation:

$$\omega_s^{-1}[dI(\omega_s)/dz] = \omega_i^{-1}[dI(\omega_i)/dz] = -\omega_p^{-1}[dI(\omega_p)/dz] \quad (18)$$

Perfect phasematching and optimum gain occurs when $\Delta k=0$. Under these conditions, the signal gain over the interaction length (single pass) becomes

$$G_S = |E_S(L)/E_S(0)|^2 - 1 = (\Gamma L)^2 \sinh^2(gL)/(gL)^2 \rightarrow \exp(2\Gamma L) \text{ for the high gain case} \quad (19)$$

and the gain bandwidth at fixed wavelength is defined by the condition :

$$|(\Delta k/2)^2 - \Gamma^2|^{1/2} L \sim \pi \quad (20)$$

Near the harmonic degenerate point $\omega_s = \omega_i = \omega_p/2$, frequency tuning of the gain response can be approximated by

$$G \sim \text{sinc}^2(\Delta k/2) \; [\; (1-\delta^2)^2] \quad (21)$$

with detuning parameter $\delta = (2\omega_s - \omega_p)/\omega_p$. The corresponding spectral bandwidth is determined by phasematching requirements (described below) and can be written:

$$\Delta\omega = (2\pi c/L)\,[n_s - n_i + (\partial n_s/\partial\omega)\omega_s + (\partial n_i/\partial\omega)\omega_i)\,]^{-1} \sim (2\pi/L)[\,\partial k_s/\partial\omega) - \partial k_i/\partial\omega]^{-1} \quad (22)$$

Note that near degeneracy, the first two terms in the denominator of $\Delta\omega$ cancel resulting in an anomalously large spectral width. Spectral width is determined primarily by the crystal length and the pump beam divergence, and the relative importance of these factors depends on the direction of the pump wave relative to the nonlinear crystal optic axis.

4.3 Phasematching and Wavelength Tuning

Spectral tuning can be achieved by varying the crystal birefringence while satisfying the energy conservation and tangential phasematching conditions. The most common way to control the refractive indices at each of the three optical frequencies involves maintaining precise angular orientation of the crystal optic axis with respect to the propagation direction of incident pump light. Phasematching at a given wavelength occurs when the value of the effective refractive index creates a condition under which $\Delta k \rightarrow 0$ is satisfied; this typically requires that the pump wavevector be shortened since $|k_p| > |k_i + k_s|$ in most cases. In general, the orientation of the nonlinear crystal for exact phasematched upconversion is given by solution to an index ellipse defined by the geometry of the parametric process relative to the preferred crystal axis

$$\Delta k = [n^i(\omega_p,\theta_p)/\lambda_p + n^j(\omega_i,\theta_i)/\lambda_i\,(\cos\phi)]\,\sec(\psi) - n^k(\omega_s,\theta_s)/\lambda_s = 0 \quad (23)$$

where ϕ denotes the phasematching angle between wavevectors $\underline{\boldsymbol{k}}_p$ and $\underline{\boldsymbol{k}}_i$, ψ denotes the phasematching angle subtending wavevectors $\underline{\boldsymbol{k}}_p$ and $\underline{\boldsymbol{k}}_s$, and angle θ_l is the orientation of the crystal axis (z) versus the wavevector associated with the lth optical plane wave. The superscript indices $\{i,j,k\}$ specify principal extraordinary or ordinary polarization components of the anisotropic refractive index. Solution of equation 22 will give the angular tuning curve or the output signal/idler frequency as a function of orientation of the optic axis of the crystal relative to the pump direction. For negative uniaxial crystals such as BBO in a type I (ϕ=0) mixing process, critical phasematching will require angular tuning in θ such that:

$$\boldsymbol{k}^{e(o)}(\omega_p) = \boldsymbol{k}^{o(e)}(\omega_s) + \boldsymbol{k}^{o(e)}(\omega_i) \quad (24)$$

For this case, signal and idler beams have identical polarization states and are orthogonally polarized to the pump beam which is polarized as an extraordinary wave. If the process is initially phasematched and collinear, tilting the crystal in the critical plane leaves the k-vectors of the *o(e)*-waves unaltered, but changes the k-vector of the *e(o)*-

wave because its refractive index changes with crystal angle. Assuming the pump beam is initially aligned such that on-axis signal fields are phasematched, as the crystal is tuned by changing its orientation (or temperature) the extraordinary index of refraction seen by pump and therefore k_p is decreased and new signal fields at increasing angles from the pump beam are now amplified as they meet the phasematching condition. Choice of *e(o)* pump orientation should be determined judiciously so that the birefringence of the material can adequately compensate for dispersion.

4.4 Acceptance Angle

Field-of-view of a nonlinear optical convertor such as an OPA is rigorously constrained by the phasematching requirements for gain. The acceptance angle $\Delta\theta$ associated with critically phasematched nonlinear mixing in a birefringent crystal is a measure of the tilt tolerance away from the perfect phasematching angle where $\Delta k=0$ and the angular dependence of the extraordinary refractive index in the critical plane which affects mixing efficiency. This angle varies inversely with crystal length and is derivable from the first null in the gain response function (Taylor series in Δk expanded about the phasematching angle) as:

$$\Delta\theta=(4\pi/L)(\partial\Delta k/\partial\theta)^{-1} \tag{25}$$

Its magnitude will have important consequences for crystal walk-off effects, Fourier imaging, and performance of off-axis tangential and radial meridians of the incident light field in the optical tranfer function.

4.5 Experimental Set-up

We have performed femtosecond parametric amplification of a monochromatic near-infrared image in a β-barium borate (BBO, d_{eff} = 2pm/V) type I (e→o+o) critically phasematched crystal (θ= 29°). In our experimental system, presented in figure 9, we cascaded two microjoule-energy BBO optical parametric amplifiers (OPA) in series, one configured as a wavelength tunable coherent light source, and the second as a quasi-ballistic gate following the transilluminated test object. The probing wavelength which interrogated the sample was derived from either the signal or the idler branch of the first OPA and both stages were sequentially pumped by second harmonic light(type I lithium triborate θ= 28°, ϕ= 90°) from the same regeneratively amplified titanium sapphire laser operating at a 250 KHz repetition rate near 800 nm to avoid timing jitter. A broadband white light continuum produced by self-focussing assisted self-phase modulation in sapphire (~.5 nJ/ 10 nm) was used to seed the first amplifier and afforded efficient spectral tuning from 470-750 nm in the signal, and .94 μm to the absorption edge of BBO near 2.4 μm in the idler, excluding the region near degeneracy. This amplifier was operated in a double pass configuration to compensate for group velocity mismatch (GVM) effects between the pump and signal/idler waves

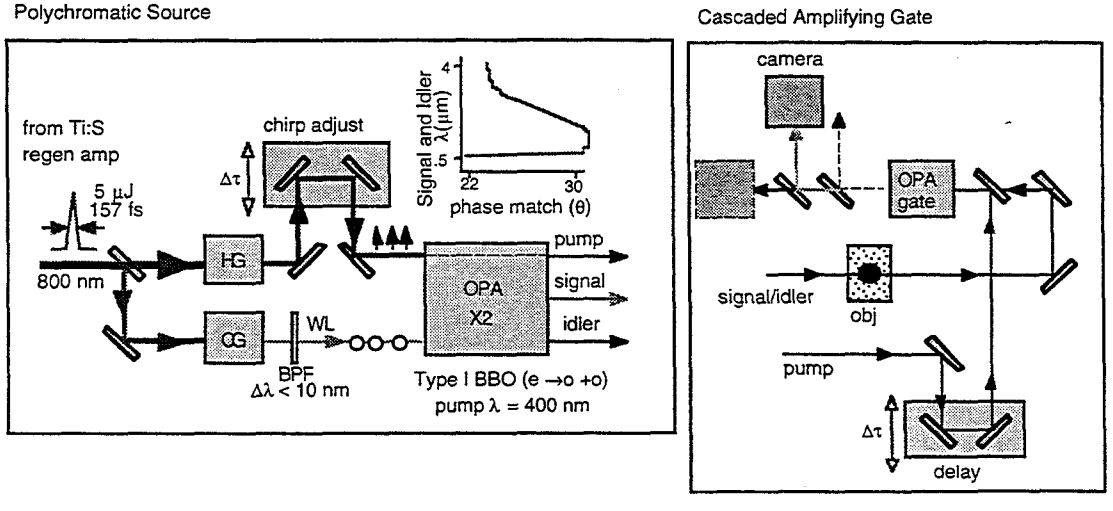

Figure 9: Experimental geometry for transillumination imaging using the optical parametric amplification process in both a wavelength tunable source and in an amplifying time-gate. Spectral tuning is accomplished byadjusting the nonlinear crystal angle.

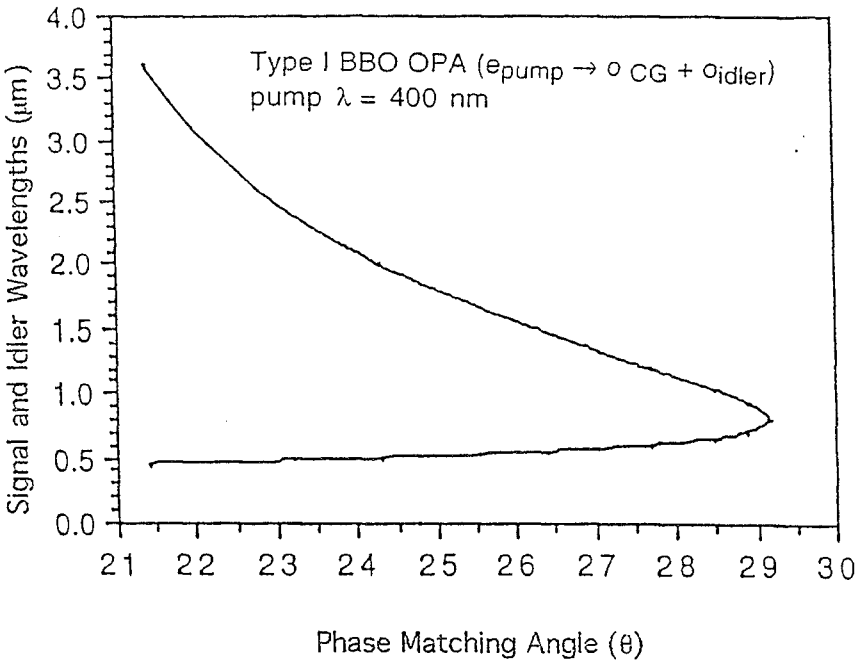

Figure 10: Critical phasematching curve for type I (e→o+o) BBO optical parametric amplification with 400 nm pump (Source: Coherent Lasers, Inc.)

($v_g^{-1} = |\partial k/\partial\omega| \sim$ 150-200 fs) and gains approaching x1000 over the white light background were routinely possible with the proper pump energy distribution in each pass. To obtain these gain levels,we adjusted the first pass to weakly saturate the amplifier so that the second pass extracted approximately 10-20% of the total pump energy.Tunable spectral ouput was generated by rotating the crystal about its phasematching axis and varying the white light delay (chirp) to allow appropriate wavelengths to temporarly overlap with the pump. The wavelength tuning curve as a function of angle ($d\lambda/d\theta$) followed the published Sellmeier equation values for type I BBO phasematching with 400 nm pumping.

As discussed earlier, type I phasematching requires orthogonal polarization states between the pump (extraordinary) and signal (or idler) waves (ordinary). Dichroic mirrors and bandpass filters were utilized to separate and combine pump and probe wavelengths with good spectral purity and collinearity in the optical layout. Typically, the signal branch exhibited near transform-limited pulses with 100-200 nJ pulse energies, ~157 fs pulsewidths, and 5-25 nm bandwidth as a function of wavelength, with lower energies and slightly longer pulses for the idler as expected. No attempt was made to actively compensate for chirp in these experiments. Figure 11 shows a representative characterization with intensity autocorrelation and a diode array spectrometer of the time-bandwidth product for pulses from the OPA in the visible far from the degenerate point. The output spectral bandwidth $\Delta\nu$ is limited by crystal phasematching and group velocity dispersion effects ($\partial^2 k/\partial\omega^2$) in the white light continuum, and is governed by

$$\Delta\nu \sim (\lambda^2 2(\ln 2)^{1/2}/\pi c)(\Gamma/L)^{1/2}|(\Delta v_g^{-1})| \qquad (26)$$

Increased temporal broadening of signal pulses observed at longer wavelengths can most likely be explained in terms of residual or slightly misadjusted chirp on the WL continuum seed arm. The measured spatial mode quality of the output beam was characterized by a Gaussian M^2 value better than 1.5 and typical peak-to-peak pulse energy jitter was ±5%.

The optimization criteria for choice of nonlinear crystal should include a large nonlinear coefficient in the required phasematching configuration and a large tolerance in divergence of the pump beam to achieve a useful acceptance angle. The nominal crystal interaction length (~1 mm) in both amplifiers (gate and source) was carefully designed to minimize spatial (Poynting) and temporal walk-off ($L<\tau\Delta v_g^{-1}$) dispersion effects detrimental to gain conversion

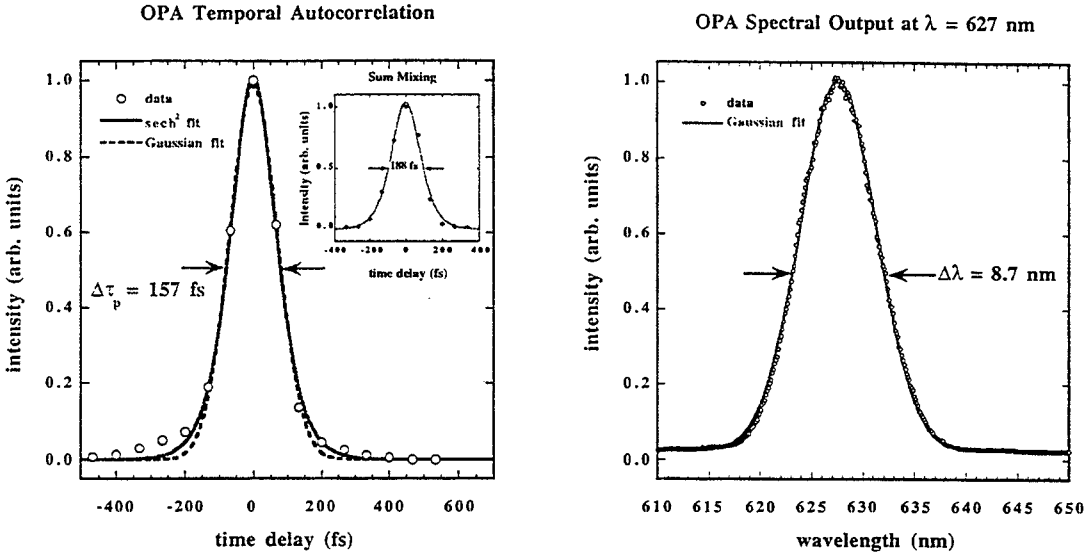

Figure 11: Time-bandwidth product and spatial profile characterization of the OPA: (a) intensity autocorrelation, insert shows cross-correlation of the OPA signal with 800 nm output of regenerative amplifier pump; (b) spectral output.

while maintaining a reasonable compromise between acceptance angle (proportional to L^{-1}) and the maximum extractable image amplification factor. Spatial walk-off due to birefringence of the nonlinear crystal in critical phasematching will limit the effective interaction length to the value

$$L_{\text{eff}} = (w_0/\rho)\text{erf}(\sqrt{\pi}L\rho/2w_0) \tag{27}$$

where w_0 is the beam waist and ρ is the double refraction angle. Similarly, temporal smearing resulting from a nonnegligible group velocity mismatch between the optical waves can limit parametric coupling over the crystal length. A collinear gate geometry was deliberately chosen in these experiments for ease of alignment and to

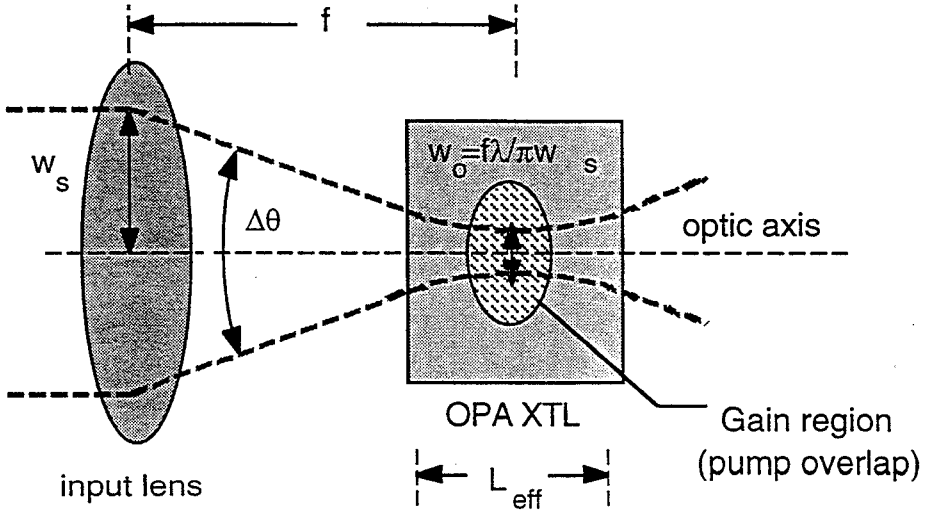

Figure 12: Optical focussing geometry in the amplifying crystal showing relationships among confocal parameters.

minimize Δk mismatch effects which can occur in crossed beam configurations and ultimately limit image spatial resolution.The well-known formulas of Kleinman and Boyd describing optimization of nonlinear optical interactions with focussed Gaussian beams were used as a starting point to set the input confocal parameters. Beam waists and depth of focus (w_0~ 80-100 μm, Rayleigh range $z_R=\pi w_0^2/\lambda$~.5 mm) were systematically adjusted for maximum spatial overlap, efficient gain, and optimum matching to the crystal angular acceptance (θdL_{BBO}=.37 milliradians-mm), subject to the self-focussing damage threshold (<50 GW/cm^2).

4.6 Gate Dynamic Range

As a preliminary benchmark experiment, we have used this system to reconstruct and enhance test images with absolute feature sizes of 65 μm/mm^2 in background optical attenuations exceeding 10^{12}. Two-dimensional amplified ballistic images of a standard Air Force resolution chart embedded between opal diffusers simulating random media were obtained for various attenuations and exposure times < 10s using a liquid nitrogen cooled 1024x1024 detector array. These diffusers are basically nonabsorbing Lambertian scatterers which attenuate the useful component of the image-bearing light by randomizing the distribution of photon paths traversing the sample and by deflecting light (via multiple scattering) from the optic axis and field-of-view of the gate. Thus the effect of the diffuser is to both effectively attenuate the beam, approximately eight orders of magnitude for 2mm of diffuser thickness, and to completely obscure any underlying image information by producing a strong diffuse afterglow or scattering halo. It should be emphasized that this process is an entirely different effect then simply attenuating the intact coherent beam; here the image is not recoverable with standard line-of-sight techniques. Images and corresponding lineouts produced with 10-100 nJ incident pulse energies at a 250 KHz repetition rate are displayed in figure 13 below.

Assuming absorption is negligible in the opal diffusers compared with the effects of diffuse scattering, the maximum measured optical density or extinction corresponds to nearly 28 scattering transport lengths; i.e., exp(-28)=exp(-$\mu_t L$). Although opal diffusers are not extended sources with a continuous variation in dielectric constant

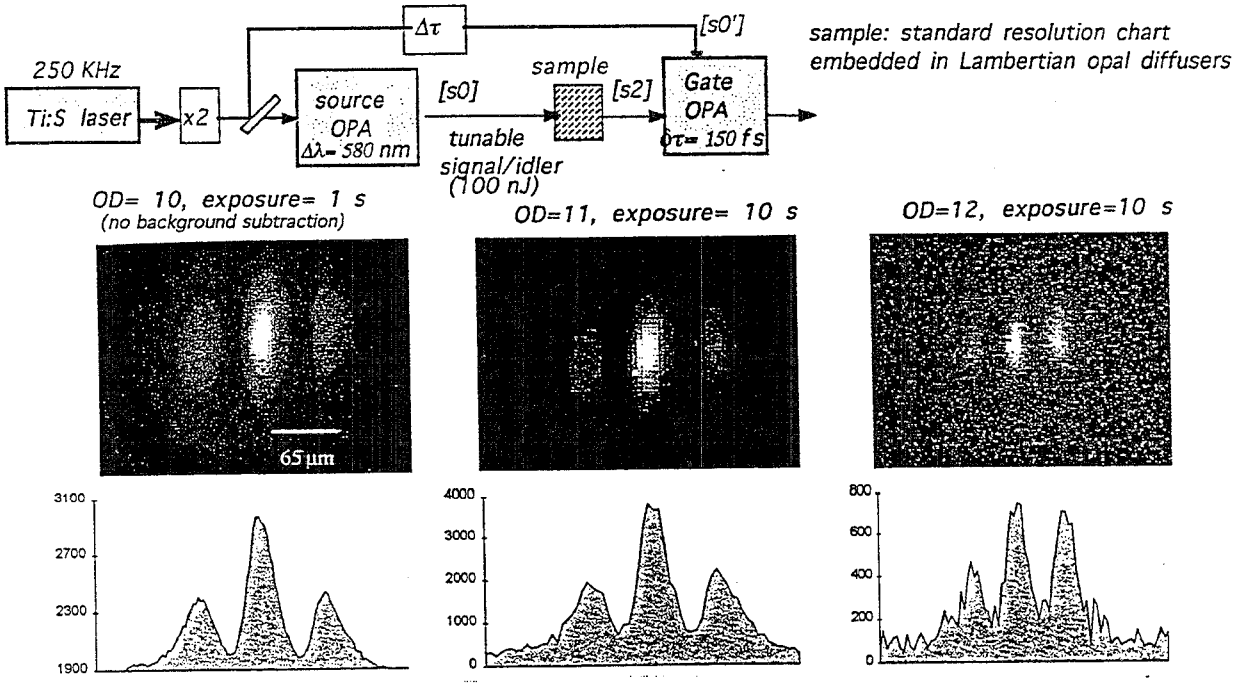

Figure 13: Ballistic images and centered lineouts obtained with the OPA system of 65 μm resolution chart features at various attenuations due to turbidity: (a) OD=10, 1 sec exposure, 4x4 binning (no background subtraction); (b) OD=11, 10 sec exposure, 8x8 binning (background subtraction); (c) OD=12, 10 sec exposure, 8x8 binning (background subtraction).

as would be the case in tissue media, the achievable dynamic range is nonetheless a significant advance for biomedical imaging applications. Assuming an inverse transport length of ~ 1 mm^{-1} ($\mu_t=\mu_a+\mu_s'$), which is a reasonable average value for fibroglandular tissue, and noting in the quasi-ballistic detection case,

$$\mu_t(\lambda) = \mu_a(\lambda) + \mu_s(\lambda) = z^{-1} \ln(I_0/I_{trans}) \quad (28)$$

this level of attenuation corresponds to a physical penetration depth (z) greater than 3 centimeters. The primary difference between tissue media and an analogous boundary diffuser will occur in the scattering anisotropy factor $g \sim \langle\cos\theta\rangle$ and in the width of the temporal distribution of the transmitted photons. Tissue exhibits both significantly more forward scattering ($g \sim .9$) and an extended optical pathlength (relative to scattering length) in comparison with an isotropic edge scatterer like opal ($g < .5$). The temporal dispersion resulting from propagation in tissue would be much wider, typically ~1 nanosecond versus < 150 ps in the opal diffuser case, and the early-arriving component would be comprised of fewer, if any, ballistic photons mandating the use of a wider time-gate or larger gate acceptance angle (FOV). In addition, the size distribution of scattering centers in the opal diffuser is much more uniform and predominantly Rayleigh-like whereas living tissue is inhomogeneous and more Mie-like in its scattering properties.

4.7 Spectral Upconversion and Amplication in the Infrared

Difference frequency in an OPA device can provide gain as well as versatile spectral tuning by virtue of the parametric coupling process between incident optical fields. Gain can be detected directly at the incident sampling wavelength or at the complimentary spectrally converted sideband which is also formed in the three-wave process as depicted in figure 14. A key advantage of combining amplification and spectral conversion functions in a single parametric gate is the ability to perform imaging at longer infrared idler wavelengths less susceptible to diffuse scattering within the water window without sacrificing the capability for efficient amplified detection at signal wavelengths within the silicon photocathode response envelope (<1100 nm). Many of these infrared wavelengths are sensitive to vibrational overtones and combination bands (OH,CH, NH) specific to metabolic changes associated with carcinogenesis and tumor pathology. Wavelength tunability will be an important aspect for optimizing absorption and scattering properties for maxuimum image contrast and detection of weak chromophores. Because the scattering coefficient appears in the exponential, small changes in its value can have a dramatic impact (orders of magnitude) on the number of available ballistic or early-arriving photons over long pathlengths in turbid media. Since the maximum permissible exposure to laser radiation increases at longer wavelengths in biological tissue higher fluences are available for imaging or alternatively, for reduced exposure times.

A cascaded experimental geometry consisting of a tunable light source based on parametric amplification in conjunction with a second OPA-based temporal gate following the illuminated object would allow full flexibility in designing an imaging system for turbid environments while matching favorable transmission windows and wavelength-dependent particle size effects in the Mie scattering function. This versatile approach was demonstrated conceptually in the laboratory with the previously described optical system using wavelengths pertinent to biomedical spectroscopy. By using the second optical parametric amplifier to simultaneously amplify and spectrally upconvert (difference mix the idler and visible pump wave) an infrared idler (λ~1.3 μm) transmitted through the sample from the first stage, we were able to substantially suppress background effects, reduce diffuse scattering ($\sigma_{scat} \sim \lambda^{-1}$) within the sample volume, enhance image formation, and improve detector dynamic range by shifting

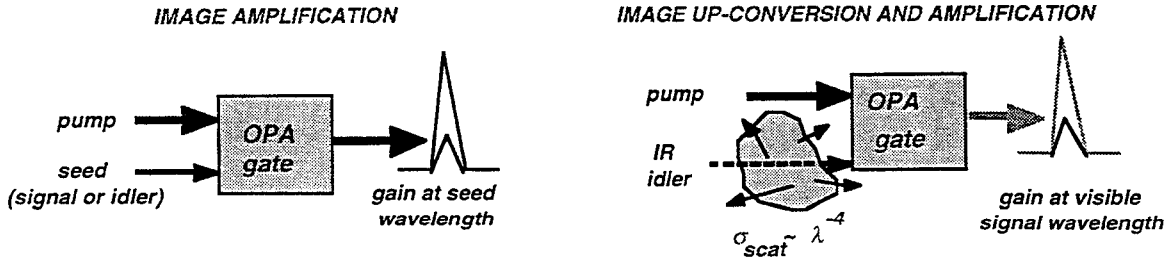

Figure 14: Direct image amplification (a) and upconversion with gain (b) are possible using an opa gate.

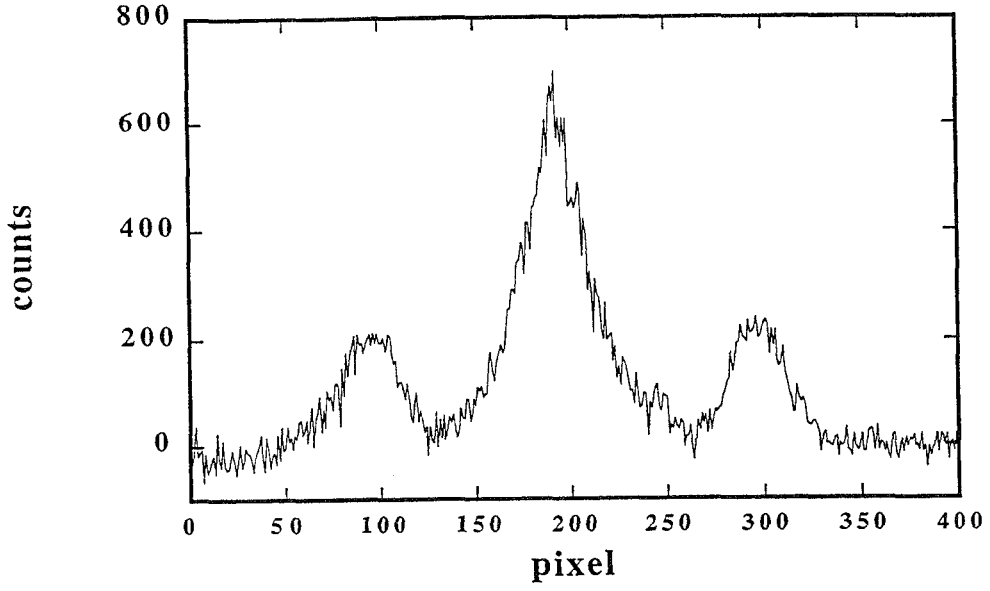

Figure 15: Pixel lineout of spectrally upconverted ($\omega_{sig} = \omega_{pump} - \omega_{idler}$), ballistically amplified resolution chart image obtained with background attenuation OD=10. Note that the idler wavelength (1.3 μm) is not directly detectable with a silicon based photocathode so the technique is zero background.

to visible signal wavelengths (λ~580 nm). Figure 15 shows the resulting image lineout obtained with an overall optical attenuation due to turbidity of 10 OD. Note that the available idler power was approximately one-quarter of of the signal case because of optical losses and wavelength scaling physics of the parametric conversion process. Longer idler wavelength schemes near 1.7 μm which would be useful for NIR detection of glucose were also shown to be possible.

4.8 Spontaneous Parametric Fluorescence Noise

An important parameter of any detection device is the noise equivalent power (NEP) which measures the amount of noise present in the absence of signal. A fundamental noise source in an optical parametric amplifier is spontaneous parametric scattering or fluorescence occuring as a result of amplification of noise photons initiated by zero-point vacuum fluctuations (noise input per mode of hω/2 in either the signal or idler channel). This nonlinear emission occurs when the initial number of photons in the signal and idler fields is zero (no seed present), and exhibits a scattering intensity higher than could be explained due to parametric mixing of the incident pump beam with quasi-phasematched blackbody radiation at the signal or idler frequency. Existence of such a phenomenon follows as a necessary consequence of quantization of the electromagnetic fields and the nonlinearity in the susceptibility of the amplifier medium. The superradiant process is a fundamental limit in high gain systems approaching $\Gamma L \sim 20$ and will lead to false images in gating applications operated under these conditions. Total parametric noise (OPN) radiated power for small-angles and near collinear phasematching can be approximated over the gain bandwidth as

$$P_{spon} = \beta L^2 P_p \int_{-\infty}^{\infty} \int_{o}^{\phi} \mathrm{sinc}^2 (\Delta k L/2)\, \phi \, d\phi \, d\omega_s = \beta L P_p \pi \phi^2 / b \qquad (29)$$

where:

$$\Delta k = k_p - k_i \cos(\psi) - k_s \cos(\phi) \sim b d\omega_s + (k_s k_p / 2k_i)\, \phi^2$$

$$b = \partial k_i/\partial \omega_i - \partial k_s/\partial \omega_s$$

$$\beta = 2h\, n_s \omega_i \omega_s^4 d_{eff}^2 / (2\pi)^2\, \varepsilon_o c^5 n_i\, n_p$$

By introducing aperture control on the angular extent of emission (i.e., ϕ dependence) between successive reduced gain stages, it should be possible to eliminate most but not all of this contribution at low light levels. Since the tuning characteristics of both spontaneous and stimulated parametric processes are based on identical frequency and wave-vector matching conditions, the spontaneous process has important application in nonlinear optics for characterization of susceptibilities and oscillator spectral tuning curves.

4.9 Diffractive Imaging with Optical Parametric Amplification

Imaging resolution characteristics of an optical parametric amplifier can be understood by considering the role of phasematching conditions in the spatial frequency domain. Each spatial frequency in the amplified bi-dimensional image, represented as a set of signal fields with k-vectors at varying angles to the pump beam, can be associated with a plane wave that propagates in a particular direction in the nonlinear gating crystal. The distribution of spatial frequencies comprising the overall plane wave superposition is then mapped by coherent diffraction to an optical transfer function incorporating the phasematching bandwidth. Parametric amplification is restricted to a small range of k-vectors by phasematching which results in the formation of a passband in the transfer function. In this sense, an optical parametric amplifier acts as a "soft" confocal aperture for spatial amplification, with the gain passband rolling off with increasing Δk corresponding to higher-order diffraction orders of the signal relative to the pump direction. Plane waves corresponding to nonzero spatial frequency are not phasematched and experience less gain. By analogy to pinhole diffraction theory, the clear aperture (D) is defined by the focussing geometry optimized for crystal acceptance angle $\Delta\theta=(4\pi/L)(\partial\Delta k/\partial\theta)^{-1}$, and the size of the gain region determines the spatial frequency cut-off $\nu_0 \sim D/\lambda$ for image formation. The number of resolution elements of the amplifer is determined by the Fresnel number $N=(A/\lambda L)^2$. and since the gain of the gate is proportional to pump intensity (power over illumination area $A \sim D^2$), the number of resolution elements at fixed gain is ultimately determined by the pump power.

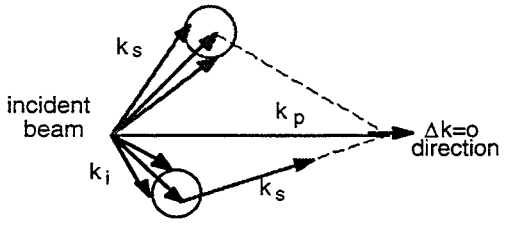

(a) Noncolinear

Image wavevectors form a cone around the mean signal k_s (null spatial frequency)

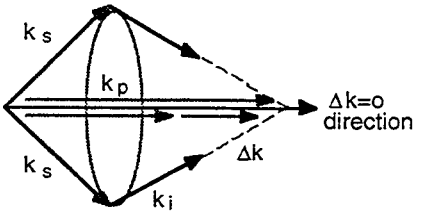

(b) Colinear

Image wavevectors k_s form a cone around the direction corresponding to incident beam and perfect phasematching direction

Figure 16: Possible three-wave phasematching geometries for diffractive imaging: (a) noncollinear, (b) collinear. In both cases, the idler formed during amplification corresponds to the opposite diffraction order.

4.10 Optical Transfer Function

Efficiency of amplification and transfer of spatial frequencies can be described by an optical transfer function (OTF) in terms of Δk mismatch, propagation vector, gain, and crystal length. The optical transfer function formalism is a mechanism for image quality evaluation which provides a complete description of the object-image relation in terms of its effect on the Fourier decomposition of the object intensity pattern. In the context of optical systems theory, the OTF is the Fourier transform of the point spread representation of the energy distribution in the focal plane of an imaging system illuminated by a uniform plane wavefront. The gain passband in the transfer function of an OPA is defined by the convolution of the gain region, principally the pump spot size, and the phasematching acceptance bandwidth $\sim |\Delta k| < \pi/2L$. This passband acts as an apodizer in the full wavevector spectrum and establishes a direct linkage between angular phasematching condition and spatial resolution. As a result, when the OPA gate is placed in the Fourier transform plane of the image, the output field is limited in extent by the effective phasematching aperture and exhibits a resolution related to the lateral size of the pump beam; in a relay imaging configuration

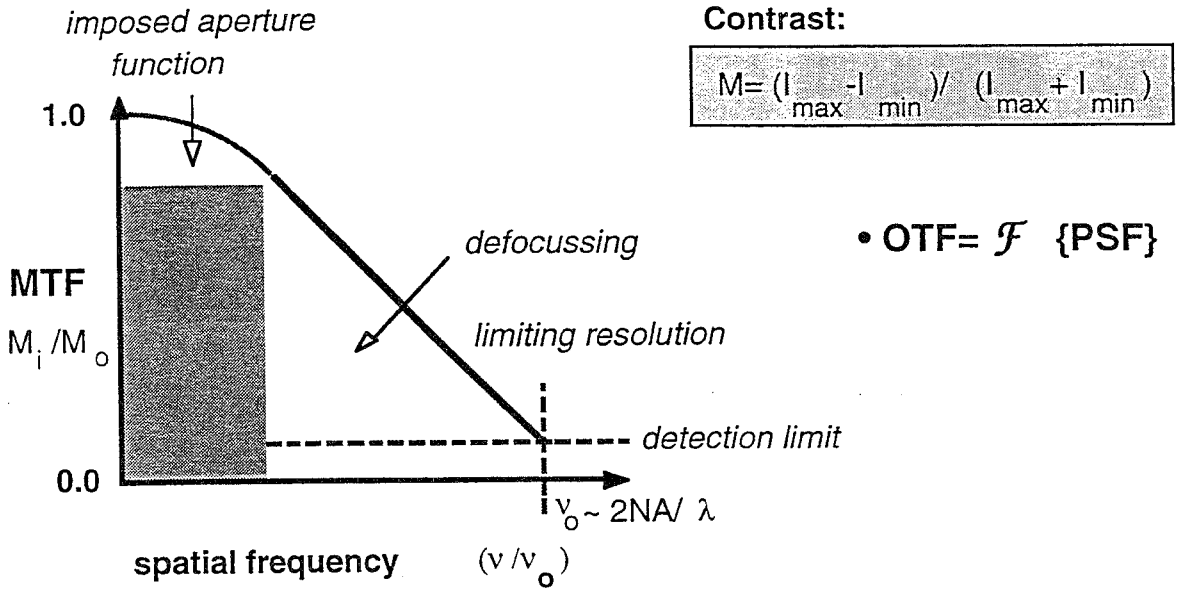

Figure 17: Evaluation of image quality by the optical transfer (OTF) formalism.

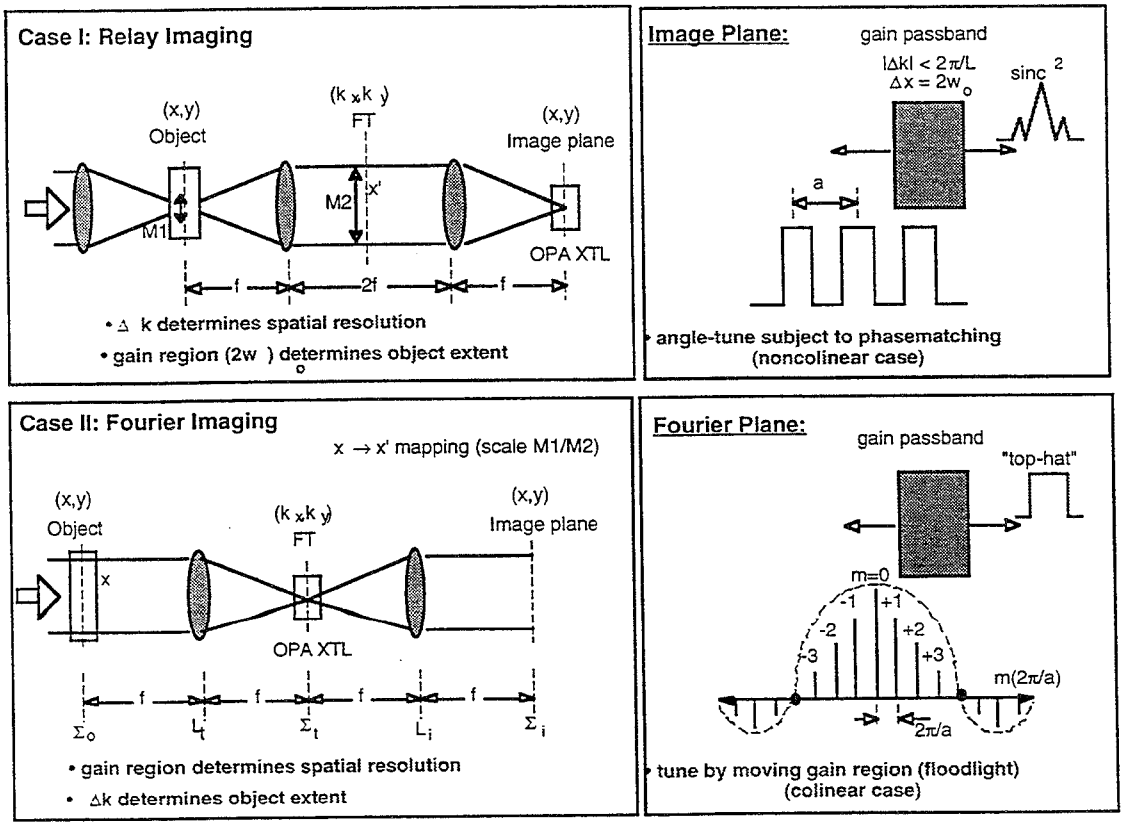

Figure 18: Relay (a) versus Fourier (b) imaging geometries showing the roles of phase mismatch (Δk) and pump beam spot size (w_o) on spatial resolution and field-of-view. The transformation plane $x \rightarrow x'$ connects the two representations with magnification scaling $M1 / M2$.

The OTF is the complex Fourier transform of the experimentally measured point spread function in the image plane and the modulation transfer function (MTF) is the real amplitude component. Aberrations such as defocussing will alter the shape and amplitude of the response function but not its general properties. such as microscopy, the roles of the previous case are reversed and one can improve resolution at the expense field-of-view by adjusting the overall magnification of the imaging system. Outside of this narrow region, transfer functions for both the signal and idler components are relatively constant over all spatial frequencies within the acceptance angle.

We directly measured the optical transfer function of spatial frequencies in our optical parametric amplifier by recording the Fourier plane image of a three-bar pattern with known spacing through the gating system. By moving the CCD camera from the conjugate image plane to an image focal plane (FT plane), either an amplified image or its corresponding spatial frequency spectrum could be clearly observed with suitable magnification The mathematical physics describing the object-image transformation relationship through a parametric amplifier is conceptualized in figure 19. The spatial frequency response data was normalized and compared to a theoretical fitting function of form

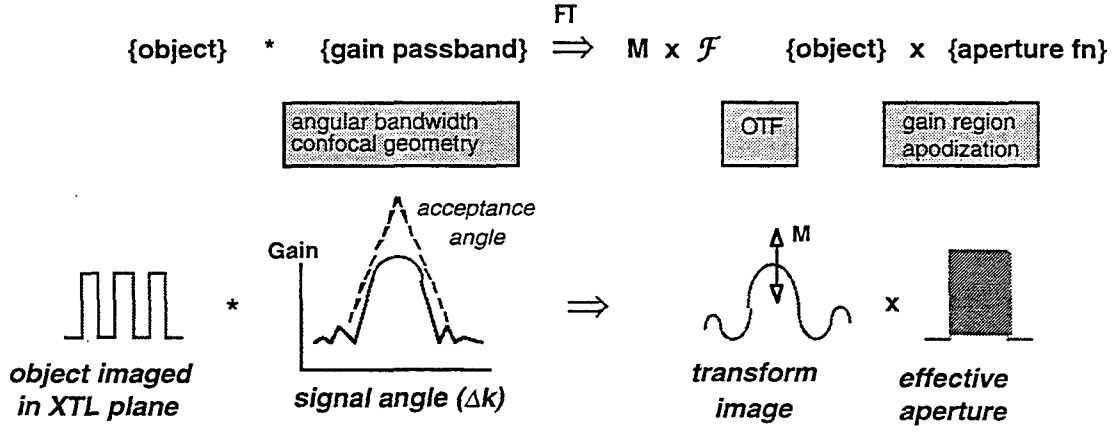

Figure 19: Physics of the object-image transformation process in the Fourier transform plane of an optical parametric amplifier, showing the effect of gain and phasematching acceptance angle on the OTF.

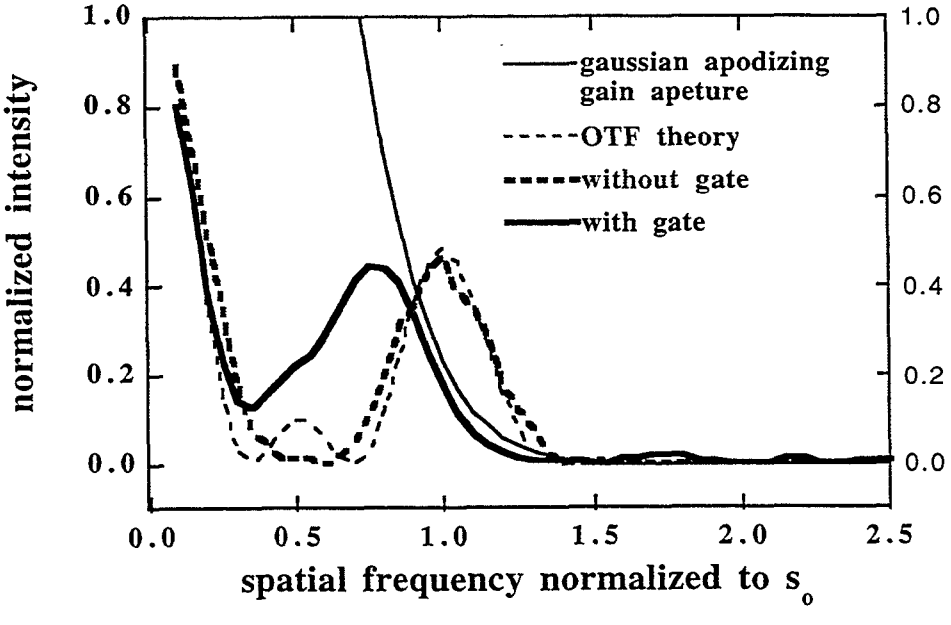

Figure 20: Measured OTF data for a 3-bar pattern through a OPA-based ballistic imaging system. Comparison with theory highlights gain and instrumental apodization features.

$$F_3(\omega) = \sin(6\pi x_1 \omega) / (2\pi\omega \cos \pi\omega x_1) \quad (30)$$

which is known to be characteristic of an idealized three-bar distribution (x_1 spacing); the cosine wave amplitude was normalized to the DC level. As displayed in figure 20, the response of the parametric gate shows both amplification and instrumental apodization originating from the gain bandwidth, when juxtaposed with the theoretical model. The observed cut-off frequency ν_0 was approximately 7.1 line pairs per millimeter. A slight astigmatism due to the walk-off plane caused there to be a difference in spatial resolution between vertical and horizontal directions (aspect ratio of 7/11).

4.11 Image Processing

Parametrically amplified ballistic imaging is capable of resolving a broad range of spatial frequencies and complex shapes with high fidelity and minimal phase distortion. In addition to performing direct image amplification, theoretical predictions made by several authors have shown that the optical parametric process can be used to selectively amplify the image spatial frequency distribution as a function of phase mismatch Δk. When the magnitude of Δk mismatch increases, maximum gain in the OTF will shift to higher spatial frequencies and the width of the passband narrows transitioning from a bandpass to an edge filter response characteristic. By manipulating the image-bearing field at the Fourier transform plane of the gate crystal relative to a nonuniform or prepatterned pump (gating) pulse, various plane wave components can be preferentially enhanced with respect to overall image intensity as a function of the gain coupling. In this mode of operation, the nonlinear gate can be configured as an active component for transmission and manipulation of optical information in coherent optical processing applications, including selective edge enhancement, character recognition, novelty filters, and correlation. Spatial amplification in the OPA does not irreversibly remove frequency information which would degrade the integrity of the image in subsequent post-processing steps as does traditional spatial filtering. By sequentially positioning nonlinear crystal gates with properly tailored pump beam enegy distributions applied to each gate operation, it is possible to combine amplification and subsequent image processing functions in a single cascaded parallel geometry. In this way, specific attributes associated with form or motion could be amplified from a weak temporally gated return and subsequently analyzed without the effects of turbidity. Note that the $\chi^{(2)}$ mechanism responsible for optical parametric amplification originates from atomic contributions to the electronic susceptibility as opposed to secondary charge carrier gratings or space charge effects so that response time is rapid (nanoseconds) compared to the photorefractive effect.

4.12 Recommendations and Improvements

Resolution and quality of image conversion in a parametric process is affected primarily by the angular aperture for phasematching and the spatially-resolved gain distribution or space-bandwidth product. Amplifier operational characteristics should be optimized for both acceptance angle (field-of-view) and overall gain efficiency. New materials with large nonlinear coefficients and less dispersion are needed to dramatically decrease angular selectivity and phasematching constraints, thereby increasing maximum image resolution and achievable penetration depths.

The nature of the solid state $\chi^{(2)}$ process inherent to parametrically amplified optical gating lends itself well to implementation with next-generation diode-pumped laser devices, particularly when employed in conjunction with micro-optical systems for focal plane efficiency enhancement. Double-pass gate geometries, or equivalently, multiple walk-off compensated crystals oriented to reverse phase slippage between extraodinary and ordinary waves can be used to improve gain performance and simultaneously increase acceptance angle. In some cases, spatial walk-off effects may be mitigated by operating in a non-critical phasematching geometry (input beam propagating at 90^o relative to the crystal optic axis) so that the angular acceptance of the crystal is higher which in turn allows tighter focussing to be used. High gain and relaxed quasi-phasematched conditions over a wide field of view can be potentially accomplished in segmented or periodically poled waveguide structures in the near infrared (eg., PPLN). Working near the degeneracy point in type I phasematching may be generally useful for polychromatic amplification applications such as time-resolved fluorescence spectroscopy where the phasematching conditions must be satisfied over a wide cone of spatial wavevectors centered on the pump direction.The ability to scan crystal phasematching orientation over a broad range of wavelengths will facilitate gated imaging of a wide variety of spectroscopic signatures, including fluorescence, photoluminescence, Raman scattering, and infrared absorption. Heterodyne signal processing techniques incorporating a gain-modulated detector and amplitude-modulated optical carrier superimposed on the pump wave may be combined with time-gating based on optical parametric amplification to further increase performance.

V. PHASE IMAGING THROUGH A BALLISTIC GATE

5.1 Binary Optics

Binary optics are hybrid optical elements exhibiting controllable refractive and diffractive imaging properties. The binary fabrication process derives its name from a multilevel processing sequence wherein discrete phase-encoded 2^N surface relief structures are patterned by integrated circuit (VLSI) manufacturing methods using iterative photomasking and etch steps. These planar phase profiles can then be used to manipulate optical wavefronts and perform agile beam steering in diverse applications ranging from amacronic focal plane sensors and aperture multiplexers, to optical interconnects (transfer optics) for photonic devices and focal plane efficiency enhancement. The arbitrary nature of the fabrication process allows essentially unlimited flexibility in constructing customized lenslet arrays as simple robust miniaturized replacements for conventional optical systems and for the creation of new unconventional components in innovative multipurpose sensors. Micro-optical devices based on this technology can be integrated with other elements such as diffraction gratings and CCD cameras to build combined spectral, intensity, and phase imaging systems which simultaneously focus and disperse light over arbitrary pupil shapes. Over the past decade, technology has sufficiently advanced to allow production of diffractive elements, hybrid refractive-diffractive elements, and refractive micro-optics which are satisfactory for use in cameras, military systems, and medical instrumentation.

Phase measurement capability will be a useful complement to ballistic imaging when refractive index variation is the dominant optical response mechanism, as in the case of translucent objects with weak absorptive contarst, turbulent shear boundaries, thermoclines, or wake fields produced in the vicinity of moving objects. A self-referencing wavefront sensor using a 40x32 lenslet array (250 μm pixel diameter) based on binary optics tyechnology has been developed at Sandia National Laboratories which is sensitive to optical path distortions (opd) approaching λ/100 and exhibits dynamic grayscale range exceeding 10^4. By incorporating such a device to measure the wavefront slope (phase gradient) and amplitude of the range-gated OPA output, it is possible to simultaneoulsy acquire phase and intensity maps of the dielectric function of an obscured object in low-visibility or turbid backgrounds.

5.2 Wavefront Sensing

Hartmann sensing offers a simple method for measuring the optical phase and intensity of laser light that has been transmitted through an aberrating medium without recourse to interferometry. In general, a Hartmann sensor consists of lenslet array with focal length (f), a pixelated camera, and a centroid algorithm that can accurately locate the positions of focal spot intensity patterns recorded by the camera. The impinging wavefront field is dissected by an array of transmissive lenslets $\{i\}$ which focus the incoming light within each subaperture onto the image plane. The sensor works on the principle that focused spots x_{ij} in the back focal plane of the microlens array will be deflected a distance $\delta=x_{ij}-x_{i0}$ away from their respective optical axes due to aberrations in the optical beam. For a given incoming spherical wave the measured tilt is approximately a linear function of position along the sensor array for

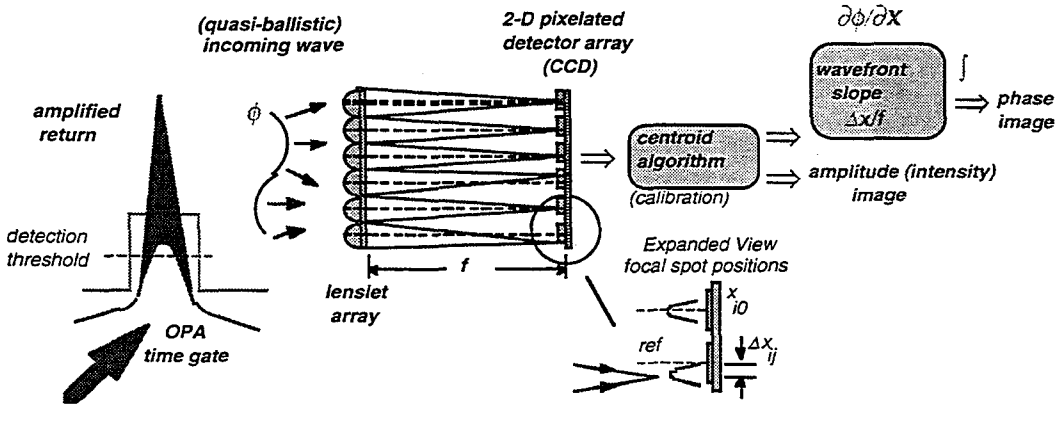

Figure 21: Simultaneous intensity and phase imaging of obscured or weak emission signatures can be achieved by integrating time-gating with an optical parametric amplifier and Shack-Hartmann wavefront sensing based on a binary-optics lenslet array.

small-angle sampling. Because light propagates in a direction normal to the wavefront, the deflection distance is proportional to the local derivative or slope $\theta \sim \delta/f$ of the optical wave front impinging on the lenslet array. Detecting the centroid position measures the gradient of optical phase along the detector axis which can subsequently be integrated to yield the optical phase distortion experienced by the beam relative to a calibration file. A digital phase reconstruction algorithm can be utilized to construct a map of complex field phasors defining the full phase front $\phi(j)$ across the measurement aperture and associated moments can be projected on a Zernike polynomial basis set. Sensitivity of the Hartmann sensor is determined by the smallest tilt differential $\Delta\theta$ that the sensor can measure between successive lenslets. Knowing the complete scalar field of the beam will facilittate detailed predictions of actual beam characteristics along its propagation path through the intervening medium.

5.3 Phasefront Measurements

We have successfully combined a binary optic wavefront sensing device with short-pulse ballistic gating using optical parametric amplification to generate spatially-resolved two-dimensional chord-integrated phase and intensity maps of various test objects in a turbid background. Standard interferometric methods for detection of phase are seriously degraded in the presence of diffuse scattering and would not be able to accurately distinguish such objects. However, a unique wavefront sensing approach overcoming these limitations can be easily implemented in a short-pulse gated imaging geometry based on optical parametric amplification by placing the lenslet array after the nonlinear crystal with appropriate relay imaging (scale magnification) and at the correct focal distance from the CCD camera. The amplification step will offset transmission losses through the mask and temporal gating of the phase measurement will eliminate random fluctuations due to stochastic turbulence along the line-of-sight. Figure 22 shows reconstructed phase and intensity contour plots of a weak 2 meter radius of curvature negative field lens placed in front of a diffuser with an overall optical density of 4 OD. The path delay in the temporally resolving gate was adjusted for the average thickness of the test lens and the overall magnification of the composite optical system allowing for the field lens defocussing was approximately 14 m which did not significantly perturb the crystal focussing geometry or gain conditions. The observed maximum phase retardation is .36 μm or slightly greater than $\lambda/2$ under these condition. This demonstrated phase measurement capability will be a useful complement to ballistic imaging when refractive index variation occurs in the absence of strong absorptive contrast. Tissue scattering is caused by a variety of substances and organelles with different refractive indices and changes in the index can change the overall scattering coefficient (Rayleigh-Ganz theory). Accurate tumor diagnosis will benefit from knowledge of both absorption and refractive index properties. Next generation sensors will combine polychromatic imaging and phase measurements with gated detection to facilitate multidimensional sampling of spectral imaging parameters (hyperspectral imaging).

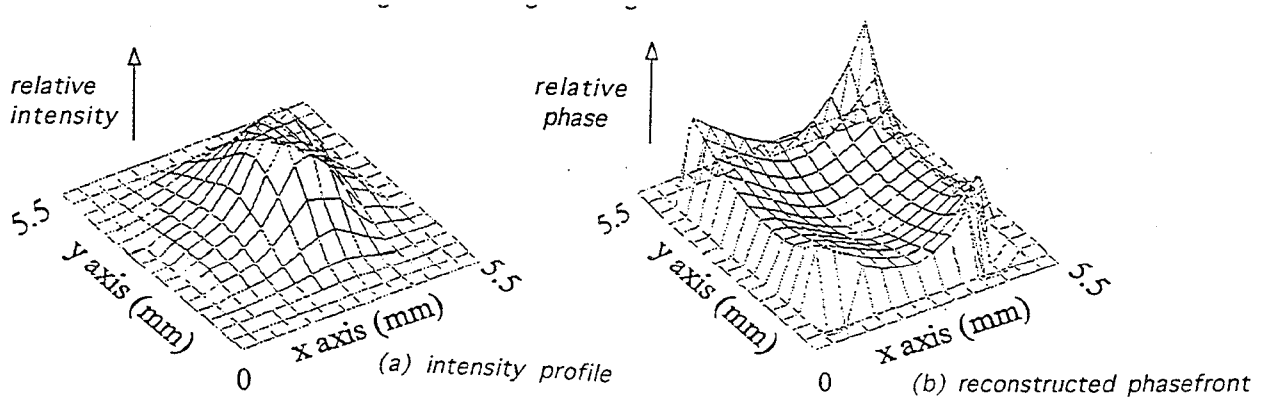

Figure 22: Detection of weak negative lens (2 m RC) as a phase object in turbid background: (a) intensity profile; (b) reconstructed phasefront based on wavefront sensor.

5.4 Beam Manipulation and Focal Plane Efficiency Enhancement

A binary optic lenslet array can be used to enhance the performance of ordinary parametric gating by increasing focal plane efficiency and reducing pulse energy requirements on the pump beam. Such an architecture will facilitate improved optical coupling of miniaturized high-brightness diode array laser devices at the nonlinear gate focal plane creating sufficient focussable intensity to trigger the parametric process in a pointwise format, while multiplex sampling a larger field-of-view. If the laser source is not pixelated as in case of a diode-pumped external cavity configuration, an aperture multiplexer can be designed which distributes the full aperture energy emitted by the pump laser into a prepatterned distribution of focussed spots without significant Fresnel coupling losses.The lenslet array can also be used to directly discretize the image formation process in the crystal Fourier transform plane, thereby increasing the effective acceptance angle without loosing overall resolution. This approach assumes that an adequate density of lenslets is utilized to sample the full scene so that the pixel density is a good approximation to a true continuous image and that a second lenslet array with comparable lens spacing to the first is aligned as a relay optic to the detector (image) plane; essentially the functional equivalent of raster scanning without moving parts. The f/# of individual lenslets should be engineered to match the crystal acceptance angle at each gain spot which is coupled to the pump light. By combining such a system with a wavefront sensor, one can create a multi-axis motion sensor with gain- spatial x,y, time gating (longitudinal or piston), and tilt- conceptually similar in operation to a quadrant detector.

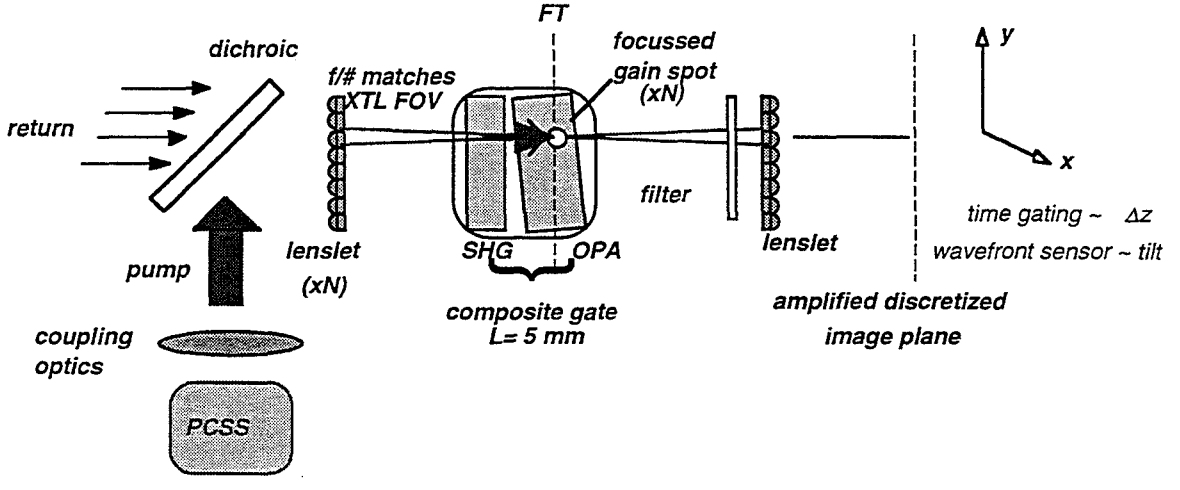

Figure.23 Image plane discretization with a lenslet array increases gate acceptance angle and facilitates pump source miniaturization.

VI. SOLID-STATE DIODE SOURCES

6.1 Monolithic Semiconductor Lasers

At Sandia National Laboratories, we have designed, fabricated, and evaluated performance characteristics of several novel miniaturized GaAs/$Al_xGa_{1-x}As$ monolithic colliding pulse modelocked semiconductor laser diode structures which emit at wavelengths 820-870 nm, incorporating several different variations of cavity design. Modelocked semiconductor laser technology offers an attractive alternative to benchtop laboratory systems owing to its inherent reliability, compactness, and wavelength versatility derived from bandgap engineering. Passively modelocked quantum well laser structures, in particular, are very promising as turn-key illumination sources for prototype biomedical imaging applications because of their low threshold currents (typically <50 ma), temperature stability, and fast modulation capability (>GHz), combined with relative ease of integration with optoelectronic circuits and endoscopic fiber optic packaging designed to eliminate optical alignment issues.

The epitaxial cross-section of the tested devices consisted of a quantum well heterostructure (GRN-SCH) embedded on a single chip with associated waveguides. Two different laser cavity designs were operationally characterized and are depicted in figure 24: (a) a linear passively modelocked CPM geometry composed of a pair of gain sections symmetrically separated by a saturable absorber ; (b) a bidirectional ring cavity incorporating a tapered Y-junction,

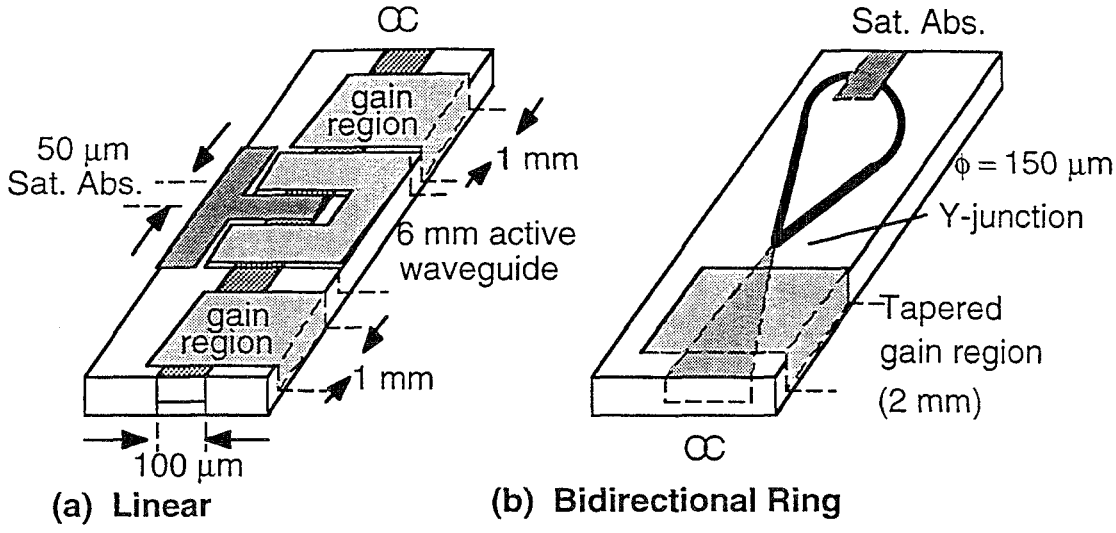

Figure 24: Cross-sectional view of monolithic semiconductor laser diode heterostructures. Linear (a) and ring (b) cavity geometries were investigated in this work.

saturable absorber, and a flared gain section. In both configurations,the purpose of the intracavity saturable absorber is to sharpen the leading edge of the recirculating pulses by preferentially passing the high energy peak of the pulses with minimum loss. Because the dynamics of the pulse-shaping mechanism is determined by the interplay of transient saturation and recovery time constants between gain and absorber sections, it is possible to generate short optical pulses with repetition rates exceeding the relaxation oscillation frequency.The pulse shaping process continues until it is ultimately limited by the intrinsic pulse broadening (dispersive) mechanisms operating cumulatively inside the laser cavity. A colliding pulse modelocking scheme accentuates this process compared to the unidirectional case by utilizing the coherent interaction of two counterpropagating pules colliding coincidently at the saturable absorber.To maximize coherent coupling between pulses, the saturable absorber is typically located at the symmetry center of the resonant cavity, and the fundamental repetition rate becomes twice the round trip frequency because there are two counterpropagating pulses travelling simultaneously in the cavity. In these lasers, active gain length was limited to approximately 2 mm to minimize group velocity dispersion and achieve the shortest possible pulses, corresponding to better longitudinal spatial resolution and gating discrimination in an eventual imaging apparatus. Typically, semiconductor lasers will emit less average power under modelocked operation versus continuous wave conditions as a result of gain saturation due to carrier depletionduring the amplification process. In a passively modelocked laser (i.e., saturable absorber), as the laser is driven to higher pulse energies pulse broadening counteracts the pulse shortening mechanism in the saturable absorber or gain modulation, resulting in poor quality pulses or even cessation of modelocked operation. The flared geometry was explored as a way to circumvent these limitations and increase power scaling without incurring gain saturation, although the effects on temporal dispersion and tranverse mode structure (which could effect fiber coupling) need to be evaluated in future experiments. A flared waveguide expands the spatial mode from a narrow region that constrains lasing to a single lateral optical mode to a wider multimode region for higher power, and consequently higher saturation energies can occur in the amplifier.

6.2 Experimental Characterization

To experimentally characterize the lasing pulse width and access the quality of modelocking, we collimated the laser output and directed in into a noncollinear second harmonic autocorrelator and optical spectrum analyzer as shown in figure 25 (a)-(d) . The measured output of a typical linear CPM cavity consisted of a modelocked train of ~ 4 ps pulses at a 10 GHz repetition rate and 5 mW average power level (100 mW peak); the intensity modulation depth and modelocking efficiency approached 100%. From the measured FWHM spectral width of the optical emission spectrum corresponding to the autocorrelation trace, the time bandwidth product $\Delta\tau\Delta\nu$ is found to be in close agreement with the transform limit value for a hyperbolic secant waveform and little evidence of chirp is found. We found empirically that the shortest pulse durations were obtained when the active waveguide was biased near threshold. One of the important factors influencing the pulsewidth of a monolithic CPM laser is the response of the

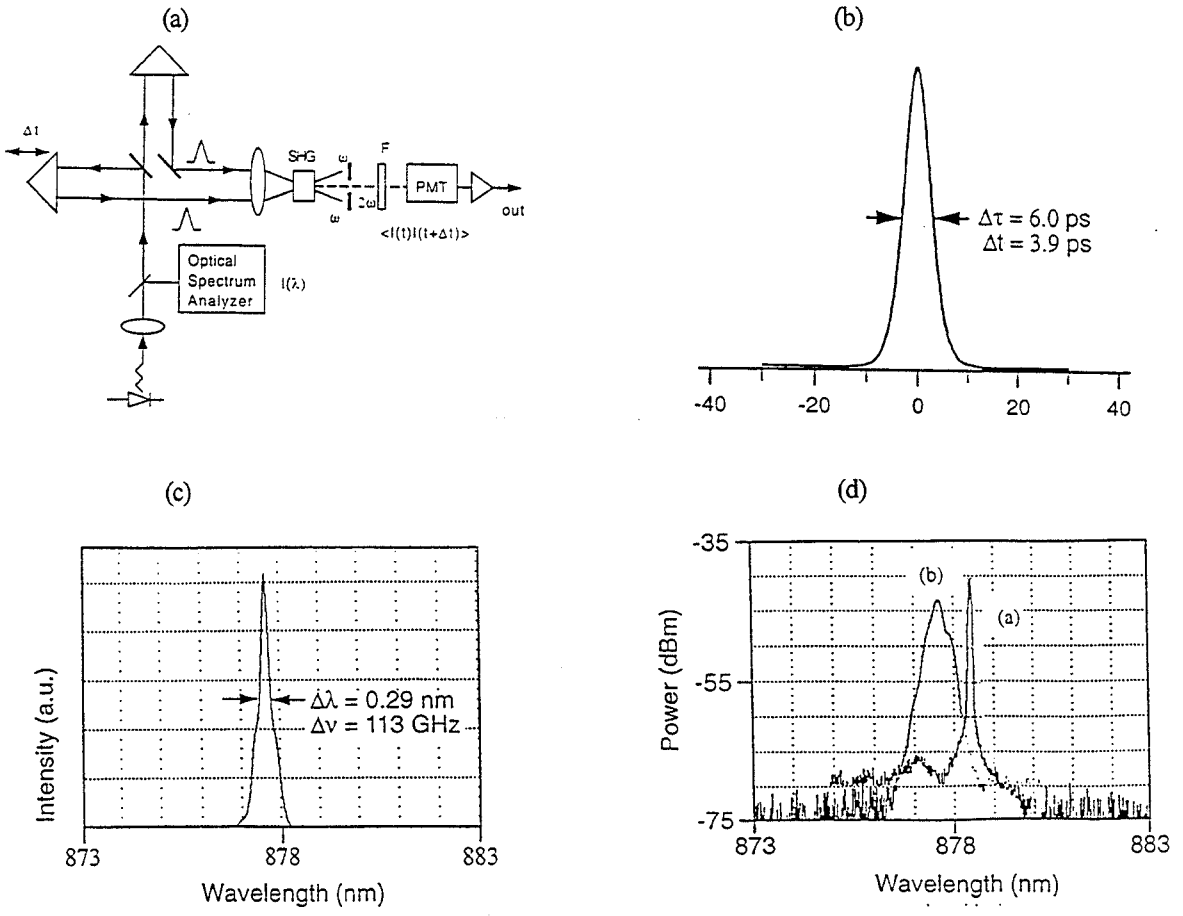

Figure 25: Optical characterization of modelocked semiconductor diode lasers: (a) experimental arrangement; (b) second harmonic autocorrelation trace for a 8.33 mm long CPM emitting a 10 GHz pulse train; (c) corresponding optical emission spectrum exhibiting transform-limited modelocking ($\Delta\tau\Delta\nu$ ~.31); (d) emission spectra for continuous and modelocked operation.

saturable absorber. Figures 25 (d) shows that when the saturable absorber bias is decreased to achieve efficient modelocking, the emission spectrum characteristically broadens to encompass several longitudinal cavity modes as expected. These results demonstrate that short pulses with very pure spectral properties and low timing jitter can be obtained by modelocking.

6.3 Future Laser Engineering Strategies

Although these preliminary results are encouraging, higher output powers will eventually be required to pump a nonlinear gate based on optical parametric amplification. One strategy toward achieving this goal is to decouple the modelocking and power amplification functions using a multi-segmented MOPA approach, thus preserving independent pulse shaping performance and adjustable saturation characteristics. A possible design would combine a passively modelocked flared waveguide laser as the oscillator stage with a tapered stripe linear waveguide amplifier. Gain switching could also be used as a mechanism to generate short pulses from semiconductor laser at high repetition rates. The process of gain switching in a laser diode is achieved by capitalizing the first period of the relaxation oscillation which is generated by switching on the laser biased just below threshold. The advantage of using a gain switched device is the inherent flexibility to change the repetition rate without modifying the cavity length. However, when the laser is suddenly switched above threhold, fluctuations in both the carrier density and the time delay between excitation and optical output can produce gain-switched pulses with signficant frequency chirp and timing jitter detrimental to precise optical coupling in the gate. A possible solution to this problem is to use a fast gain-switched photoconductive array as the flashlamp for an external micro-cavity laser operated just below threshold. It is also possible to synchronize optical pulses by hybrid modelocking using externally modulated rf sections.

VII. CONCLUSIONS

The transillumination imaging approach described in this contribution incorporates an optically-gated image intensifier with high dynamic range ($>10^{10}$) based on parametric amplification The overall system design is both versatile and compact, integrating gain (amplification), wavelength tunability, and temporal gating functions in a single package. The amplifying gate configuration achieves a high level of coherent discrimination (polarization, spatial, temporal) against time-delayed diffusely scattered noise while maintaining high transmission efficiency of the coherent image- bearing component as a function of gain. Expanded dynamic range characteristics offset previous limitations on the detectability of objects obscured by pervasive multiple scattering while preserving full image fidelity. Alternatively, the improved dynamic range means previous sensitivity levels and penetration depths are achievable with a considerably smaller laser front-end making miniaturization possible. The all-optical nature of the gain process provides for short variable gate durations continuously adjustable by the pump pulsewidth for maximum contrast and diffuse light rejection, and the parametric coupling process between incident light fields allows for spectral conversion of 2-D images with gain and zero background. The operating wavelength can be independently adjusted over the crytsal phasematching curve (450nm- 2.2 μm) to optimize the response of the imaging apparatus for variable spectral properties in the measurement medium, and in combination with a wavefront sensor the time-gated amplification process can be adapted to simultaneously acquire phase and amplitude attributes of the intrinsic dielectric function. This phase measurement capability is to our knowledge unique and will be useful when refractive index variation dominates absorption contrast in the optical response. The system is fully compatible with realtime coherent optical processing and the frequency agile solid state architecture inherent to this format will benefit from and is fully adaptable to evolving diode laser devices.

Optical parametric gating represents an important application of nonlinear optics to image processing and visualization of ultrafast phenomena in turbid media such as biological tissue. By defeating many of the traditional dynamic range issues which have plagued tissue imaging in the past, the practical realization of an optical tomography based on time-gated parametric amplification could be a promising alternative to conventional radiographic imaging modalities and dramatically increase effectiveness of early intervention strategies to detect carcinomas. Since wavelength and pulsewidth considerations for transillumination measurements of this type overlap well with evolving solid-state laser technologies, including miniaturized diode sources and integrated photonic optical sensing elements, the development of a biomedical imaging apparatus based on such an architecture could be a significant step toward producing a versatile clinical instrument. Although much of the research aimed toward imaging through turbid media is pertinent to medical spectroscopy, it is also isomorphic to a number of problems of long standing such as atmospheric and oceanographic lidar in clouds and coastal seawater, and nondestructive subsurface metrology of composite layers or buried interfaces- cases where the measurement object is unobservable using conventional optical line-of-sight techniques.

VIII. ACKNOWLEDGEMENTS

The authors would like to acknowledge partial funding from a Laboratory Directed Research and Development (LDRD) grant and useful scientific discussions with Robert Michie and Rick Spielman. We would also like to express appreciation to Daniel R. Neal for the use of wavefront sensor hardware and supporting analysis software, and to Mark Kimmel who provided technical assistance in the early stages of this project.

IX. REFERENCES

9.1 Breast Cancer and Optical Mammography

B. Monsees, J.M. Destouet, and W.G. Totty, "*Light scanning versus mammography in breast cancer detection,*" Rad., vol. 163, p. 463, 1987.

R.R. Alfano, P.P. Ho, and K.M. Yoo, "*Photonics design and solution: Optical imaging versus x-ray for breast cancer screening,*" Photonics Spectra, vol. 26, p. 109, 1992.

B. Drexler, J.L. Davis, and G. Schofield, "*Diaphanography in the diagnosis of breast tissue,*" Rad. vol. 157, p. 41, 1985.

D.J. Wartmough, "T*ransillumination of breast tissues: factors governing optical imaging of lesions,*" Radiology, vol. 147, p. 89, 1983.

M. Swift, D. Morrell, R.B. Massey, and C.L. Chase, "*Incidence of cancer in 161 families affected by ataxia-telangiectasia,*" New England J. Med., vol. 325, p. 1831, 1991.

S.A. Feig, "*Decreased breast cancer mortality through mammographic screening: Results of clinical trial,*" Radiology, vol. 167, p. 659, 1984.

American College of Physicians, "*The use of diagnostic tests for screening and evaluation of breast lesions,*" Ann. Inter. Med., vol. 103, p. 147, 1985.

P.M. Gullino, "*Natural history of breast cancer- progression from hyperplasia to neoplasia as predicted by angiogenesis,*" Cancer, vol. 39, 2697, 1977.

S. Shapiro, W. Venet, P. Strax, et al, "*Ten-to-fourteen- year effect on screening and breast cancer mortality,*" J. Natl. Cancer Inst., vol. 69, p. 349, 1982.

J.W. Berg, "*Clinical implications of risk factors for breast cancer,*" Cancer, vol. 53, p. 589, 1984.

R. Bedwani, J. Vana, and D. Rosner, "*Management and survival of female patients with minimal breast cancer,*" Cancer, vol. 47, p. 2769, 1981.

B. Lundgren, "*Observation on growth rate of breast carcinoma and its possible implication for lead time,*" Cancer, vol. 40, p. 1722, 1977.

C.C. Boring, T.S. Squires, and T. Tong, *Cancer Statistics 1992*, CA-A Cancer J. Clinic., vol. 42, p. 19, 1992.

J.R. Harris, M.E. Lippman, U. Umberto Veronesl, et al, *Breast Cancer* (first of three parts), New England J. Med., vol. 327, p. B19, 1992.

U.S. Dept. of Health Education and Welfare, *Cancer Patient Survival* Report #5, DHEW (NIH) 77-922, Washington DC, p. 164, 1976.

9.2 Optical Spectroscopy of Neurological Function

P.W. McCormick, et al, "*Noninvasive Cerebral Optical Spectroscopies for monitoring cerebral oxygen delivery and hemodynamics,*" Crit. Care Med., vol. 19, p. 89, 1991.

L.O. Svaasand and R. Ellingsen, "*Optical properties of human brain,*" J. Cereb. Blood Flow Metabol., vol. 3, p. 293, 1983.

J.S. Wyatt, A.D. Williams, D. Azzopardi, and E.O.R. Reynolds, "*Magnetic resonance and near infrared spectroscopy for investigation of perinatal hypoxic-ischemic brain injury,*" Arch. Dis. Child., vol. 64, p. 953, 1989.

E.C. Benzel and G.C. Wild, "*Biochemical mechanism of post-traumatic neural injury,*" Neurolog. Surg. , vol. 2, p. 95, 1991

P.W. McCormick, M. Stewart, G. Lewis, M. Dujouny, and J.I. Ausman, "*Intracerebral penetration of infared light,*" J. Neurosurg., vol. 76, p. 315, 1992.

F.F. Jobsis, "*Noninvasive infrared monitoring of cerebral and myocardial oxygen suffering and circulation parameters,*" Science, vol. 198, p. 1264, 1975.

K.M. Hebeda, T. Meousky, J.F. Beek, J.G. Wolberg, and M.J.C. van Gemert, "*Light propagation in the brain depends on nerve fiber orientation,*" Neurosurg., vol. 35, p. 720, 1994.

9.3 Tissue Optical Properties

R. Marchesini, A. Bertoni, S. Andreola, E. Melloni, A.E. Sichirollo, "*Extinction and absorption coefficient and scattering phase function of human tissue in vivo,*" Applied Optics, vol. 28, p. 2318, 1989.

W.F. Cheong, S.A. Prahl, and A.J. Welch, "*A review of the optical properties of biological tissue,*" IEEE J. Quantum Elec., vol. 26, p. 2166, 1990.

A.J. Welch, G. Yoon, and M.J.C. van Gemert, "*Practical models for light distribution in laser irradiated tissue,*" Lasers in Surgery and Medicine, vol. 6, p. 488, 1987.

9.4 Light Propagation in Diffusely Scattering Media

D.T. Delpy, M. Cope, P. van der Zee, S.R. Arridge, S.Wray, and J.S. Wyatt, "*Estimation of optical pathlength through tissue from direct time-of-flight measurement,*" Phys. Med. Biol., vol. 33, p. 1433, 1988.

D.T. Delpy, et al, "*Quantification of pathlength in optical spectroscopy,*" Adv. Exp. Med. Biol., vol. 248, p. 41, 1989.

B.C. Wilson, M.S. Patterson, S.T. Flock, D.R. Wyman, "T*issue optical properties in relation to light propagation model and in vivo dosimetry,*" in Photon Migration in Tissue, B. Chance ed.,(Plenum) p. 24, 1989.

M.S. Patterson, B.C. Wilson, and D.R. Wyman, "T*he propagation of optical radiation in tissues I. Models of radiation transport and their application,*" Lasers Med. Sci. vol. 6, p. 155, 1991.

B.C. Wilson and G. Adam, "*A Monte Carlo Model for the absorption and flux distributions of light in tissue,*" Med. Phys., vol. 10, 824, 1983.

M.S. Patterson, S.J. Madsen, J.D. Moulton, and B.C. Wilson,"D*iffusion equation representation of photon migration in tissue,*" IEEE MTT-S Digest, p. 905, 1991.

9.5 Frequency-Resolved Imaging Methods (Photon Density Waves)

E.B. de Haller, "T*ime-resolved transillumination and optical tomography,*" Journal of Biomedical Optics, vol. 1, pp. 7 , 1996.

R.G. Tromberg, L.O. Svaasand, T.T. Tsay, and R.C. Haskell, "*Properties of photon density waves in multiply scattering media,*" Applied Optics, vol. 32, p. 607, 1993.

L.O. Svaasand, B.J. Tromberg, R.C. Haskell, T.T. Tsay, and M.W. Berns, "*Tissue characterization and imaging using photon density waves,*" Opt. Eng., vol. 32, p. 258, 1993.

F. Fishkin, E. Gratton, M.S. van de Ven, and W.W. Mantulin, "*Diffusion of intensity modulated near infrared light in turbid media,*" SPIE, vol. 1431, p. 122, 1991.

D.A. Boas, M.A. O'Leary, B. Chance, and A.J. Yodh, "*Scattering and wavelength transduction in diffuse photon density waves,*" Phys. Rev. E, vol. 47, p. 2999, 1993.

A. Yodh and B. Chance, "*Spectroscopy and imaging with diffuse light,*" Physics Today, March issue, p. 34, 1995.

A. Knuttel, J.M. Schmitt and J.R. Knutson, "*Spatial localization of absorbing bodies by interfering diffuse photon density waves,*" Applied Optics, vol. 32, p. 381, 1993.

J.M. Schmitt, et al, "*Interference of diffuse light waves,*" JOSA, vol. 9, p. 1832, 1992.

D.A. Benaron, et al, "*Noninvasive estimation of cerebral oxygenation and oxygen consumption using phase shift spectrophotometry,*" Proc. IEEE Eng. Med. Biol., vol. 12, p. 2004, 1990.

E.M. Sevick, J.R. Lakowicz, H. Szmacinski, K. Nowaczyk, and M.L. Johnson, "*Frequency domain imaging of absorber obscured by scattering,*" J. Photochem. Photobiol. B: Biol, vol. 16, p. 169, 1992.

S.L. Jacques, "*Principles of phase-resolved optical instrumentation,*" SPIE, vol. 1525, p. 143, 1991.

M.S. Patterson, J.D. Moulton, B.C. Wilson, K.W. Berndt, and J.R. Lakowicz, "*Frequency domain reflectance for the determination of the scattering and absorption properties of tissue,*" Applied Optics, vol. 30, p. 4474, 1991.

F.Liu, K.M. Yoo, and R.R. Alfano, "*Should photon flux or photon density be used to describe the temporal profile of scattered ultrashort laser pulses in random media?,*" Optics Letters. vol. 18, p. 432, 1993.

9.6 Time-Resolved Imaging Methods

L. Feng, K.M. Yoo, and R.R. Alfano, "*Ultrafast laser-pulse transmission and imaging through biological tissue,*" Applied Optics, vol. 32, p. 554, 1993.

K.M. Yoo and R.R. Alfano, "*Time-resolved coherent and incoherent components of the forward light scattering in random media,*" Optics Letters, vol. 15, p. 320, 1990.

K.M. Yoo, F. Liu, and R.R. Alfano, "*Biological materials probed by the temporal and angular profiles of backscattered laser pulses,*" JOSA B, vol. 7, p. 1685, 1990.

D.A. Benaron and D.K. Stevenson, "*Optical time of flight and absorbance imaging of biological tissue,*" Science, vol. 259, p. 1463, 1993.

B.B. Das, K.M. Yoo, and R.R. Alfano, "*Ultrafast time-gated imaging in thick tissue: a step towards optical mammography,*" Optics Letters, vol. 18, p. 1092, 1991.

L. Wang, P.P. Ho, C. Liu, G. Zhang, and R.R. Alfano, "*Ballistic 2-D imaging through scattering walls using an ultrafast optical Kerr gate,*" Science, vol. 253, p. 769, 1991.

L. Wang, P.P. ho, X. Liang, H. Dai, and R.R. Alfano, "*Kerr-Fourier imaging of hidden object in thick turbid media,*" Optics Letters, vol. 18, p. 241, 1993.

Q.Z. Wang, X. Liang, L. Wang, P.P. ho, and R.R. Alfano, "*Fourier spatial filter acting as temporal gate for light propagating through a turbid media,*" Optics Letters, vol. 20, p. 1498, 1995.

K.M. Yoo, Q. Xing, and R.R. Alfano,"*Imaging optics in highly scattering media using femtosecond second harmonic generation cross-correlation time gating,*" Optics Letters, vol. 16, p. 1019, 1991.

F.A. Marks, H.W. Tomlinson, and G.W. Brooksby, "*A comprehensive approach to breast cancer detection using light: photon localization by ultrasound modulation and tissue characterization by spectral discrimination,* " SPIE, vol. 1888, p. 500, 1993.

N.H. Abramson and K.K. Spears, "Single pulse light-in-flight recording by holography," Applied Optics, vol. 28, p. 1834, 1989.

E. Leith, C. Chen, H. Chen, D. Dilworth, J. Lopez, J. Rudd, P.C. Sun, J. Valdmanis, and G. Vossler, "*Imaging through scattering media with holography,*" JOSA, vol A9, p. 1148, 1992.

H. Chen, Y. Chen, D. Dilworth, E. Leith, J. Lopez, and J. Valdmanis, "T*wo-dimensional imaging through diffusing media using 150 femtosecond gated electronic holography techniques,*" Optics Letters, vol 16, p. 487, 1991.

K.G. Spears, J. Serafin, N.H. Abramson, X. Zhu, and H. Bjelkhagen, "*Chrono-coherent imaging for medicine,*" *IEEE Trans.* Biomedical Engineering, vol. 36, p. 1210, 1989.

C. Yan and J.C. Diels, "*Imaging with femtosecond pulses*," Applied Optics, vol. 31, p. 6869, 1992.

S.C.W. Hyde, N.P. Barry, R. Jones, J.C. Dainty, P.M.W. French, M.B. Klein, and B.A. Wechsler, "*Depth-resolved holographic Imaging through scattering media by photorefraction,*" Optics Letters, vol. 20, p. 1331, 1995.

J.C. Hebden and R.A. Kruges, "*Transillumination imaging performance: a time-of-flight imaging system,*" Medical Physics, vol. 17, p. 351, 1990.

E.B. de Haller, C. Depeursinge, and C.Y. Genton, "*Resolution of time-resolved breast transillumination in vitro measurement compared with theoretical predictions,*" Opt. Eng., vol. 34, p. 2084, 1995.

J.A. Moon, R. Mahon, M.D. Duncan, and J. Reintjes, "T*hree-dimensional reflective image reconstruction through a scattering medium based on time-gated Raman amplification,*" Optics Letters, vol. 19, p. 1234, 1994.

M. Bashkansky, C.L. Alder, and J. Reintjes, "*Coherently amplified Raman polarization gate for imaging through scattering media,*" Optics Letters, vol. 19, p. 350, 1994.

M.D. Duncan, R. Mahon, L.L. Tankersley, and J.F. Reintjes, "*Time-gated imaging through scattering media using stimulated Raman amplification,*" Optics Letters, vol. 16, 1868, 1991.

J.G. Fujimoto, S. De Silvestri, E.P. Ippen, "*Femtosecond optical ranging in biological systems*," Optics Letters, vol. 11, p. 150, 1986.

M.R. Hee, J.A. Izatt, J.M. Jacobson, and J.G. Fujimoto, "*Femtosecond transillumination optical coherence tomography,*" Optics Letters, vol. 18, p. 950, 1993.

S. Andersson-Engels, R. Berg, S. Svanberg, and O. Jarlman, "T*ime-resolved transillumination for medical diagnostics,*" Optics Letters, vol. 15, p. 1179, 1990.

S. Andersson-Engels, R. Berg, A. Persson, and S. Svanberg, "*Multispectral tissue characterization with time-resolved detection of diffusely scattered white light,*" Optics Letters, vol. 18, p. 1697, 1993.

D.A.. Benaron, M.A. Lenox, and D.K. Stevenson, "*2-D and 3-D images of thick tissue using time constarined time-of-flight and absorbance (tc-TOFA) spectrophotometry,*" SPIE, vol. 164, p. 35, 1992.

M. Toida, M. Kondo, T. Ichimura, and H. Inaba, "*Two-dimensional coherent detection imaging in multiple scattering media based on directional resolution capabilities of the optical heterodyne method,*" Applied Physics, vol. B, 1991.

J.C. Hebden and K.S. Wong, "*Time-resolved optical tomography,*" Applied Optics, vol. 32, p. 372, 1993.

J.C. Hebden, "*Evaluating the spatial resolution performance of a time-rsolved imaging system,*" Med. Phys., vol. 19, p.1081, 1992.

A.M. Weiner, J.P. Heritage, R.N. Thurston, "*Synthesis of phase-coherent picosecond optical square pulses,*" Optics Letters, vol. 11, p. 153, 1986.

9.7 Optical Parametric Amplifiers

M.K. Reed, M.K. Steiner-Shepard, M.S. Armas, and D.K. Negus, "*Micro-joule ultrafast optical parametric amplifier,*" JOSA B, vol. 12, p. 2229, 1995.

G.W. Faris and M. Banks, "*Upconverting time gate for imaging through highly scattering media,*" Optics Letters, vol. 19, p. 1813, 1994.

J. Watson, P. Georges, T. Lepine, B. Alonzi, and A. Brun, "*Imaging in diffuse media with ultrafast degenerate optical parametric amplifier,*" Optics Letters, vol. 20, p. 231, 1995.

F. Deraux and E. Lantz, "*Parametric amplification of a polychromatic image,*" JOSA, vol. B12, p. 2245, 1995.

F. Devaux and E. Lantz, "*Transfer function of spatial frequencies in parametric image amplification: experimental analysis and application to picosecond spatial filtering,*" Optics Communications, vo. 114, p. 225, 1995.

R.N. Bracewell, *The Fourier Transfrom and its Application*, McGraw-Hill (New York), 1986.

A. Gavrielides, P. Peterson, and D. Cardimona, "*Diffractive imaging in three-wave interaction,*" J. Applied Physics, vol. 62, p. 2640, 1987.

P.A. Laferriere, C.J. Wetterer, L.P. Schelonka, and M.A. Kramer, "*Spatial-frequency selection using downconversion optical parametric amplification,* " J. Applied Physics, vol. 65, p. 3347, 1989.

J.W. Goodman, *Introduction to Fourier Optics*, McGraw-Hill (New York), 1988.

Y.R. Shen, T*he Principles of Nonlinear Optics*, John Wiley & Sons (New York), 1984

S.M. Cameron, D.E. Bliss, and M.W. Kimmel, "*Gated frequency-resolved optical imagig with an optical parametric amplifier for medical applications,*" SPIE, vol. 2679, p. 195, 1996.

9.8 Wavefront Sensing

L. McMackin, B. Masson, N. Clark, K. Bishop, R. Pierson, and E. Chen, "*Hartmann wavefront sensor studies of dynamic organized structures in flow fields,*" AIAA Journal, vol. 33, p. 2158, 1995.

D.R. Neal, J.D. Mansell, J.K. Gruetzner, R. Morgan, and M.E. Warren, "*Specialized wavefront sensor for adaptive optics,*" SPIE Proceedings Adaptive Optical Systems and Applications, vol. 2534, p.338, 1995.

9.9 Semiconductor Diode Lasers

R. Berg, O. Jarlman, and S. Svanberg, "*Medical transillumination imaging using short pulse diode laser,*" Applied Optics, vol. 32, p. 574, 1993.

P.J. Delfyett, L.T. Florez, N. Stoffel, T. Gmitten, N.C. Andreadakis, Y. Silberberg, J.P. Heritage, and G.A. Alphonse, "*High power ultrafast laser diodes,*" IEEE J. Quantum Elec., vol. 28, p. 2203, 1992.

Y.K. Chen and M. C. Wu, "*Monolithic colliding-pulse mode-locked quantum well laser,*", IEEE J. Quantum Elec., vol. 28, p. 2176, 1992.

M.C. Wu, Y.K. Chen, T. Tanbun-Ek, R.A. Logan, M.A. Chin, and G. Raybon, "*Transform limited 1.4 picosecond optical pulse from a monolithic colliding pulse modelocked quantum well laser,*" Appl. Phys. Lett., vol. 57, p. 759, 1990.

Distribution:

Copies	Mail Stop	Name, Org.
25	1423	S. M. Cameron, 1128
10	1421	D. E. Bliss, 1152
1	1423	G. N. Hays, 1128
1	1421	G. A. Samara, 1152
1	1427	S. T. Picraux, 1100
1	0513	R. Eagan, 1000
1	1194	R. B. Spielman, 9573
1	1194	D. H. McDaniel, 9573
1	1178	R. A. Hamil, 9512
1	1153	F. J. Zutavern, 9323
1	1190	D. L. Cook, 9500
1	0151	G. Yonas, 9000
1	9018	Central Tech Files, 8940-2
5	0899	Technical Library, 4414
2	0619	Review and Approval Desk, 12690 for DOE/OSTI
1	0161	Patents (G. H. Libman)
3	1436	LDRD Office, 1011